

# The impact of using assimilated Aeolus wind data on regional WRF-Chem dust simulations

Pantelis Kiriakidis<sup>1</sup>, Antonis Gkikas<sup>2,6</sup>, Georgios Papangelis<sup>2</sup>, Theodoros Christoudias<sup>1</sup>, Jonilda Kushta<sup>1</sup>, Emmanouil Proestakis<sup>2</sup>, Anna Kampouri<sup>2</sup>, Eleni Marinou<sup>2</sup>, Eleni Drakaki<sup>2</sup>, Angela Benedetti<sup>3</sup>, Michael Rennie<sup>3</sup>, Christian Retscher<sup>5</sup>, Anne Grete Straume<sup>4</sup>, Alexandru Dandocsi<sup>5</sup>, Jean Sciare<sup>1</sup>, and Vasilis Amiridis<sup>2</sup>

<sup>1</sup>Climate and Atmosphere Research Center, The Cyprus Institute, 2121 Nicosia, Cyprus

<sup>2</sup>National Observatory of Athens, Nymphs Hill 118 10, Athens, Greece

<sup>3</sup>European Centre for Medium Range Weather Forecasts, RG2 9AX, Reading, United Kingdom

<sup>4</sup>European Space Agency, 2201 AZ, Noordwijk, Netherlands

<sup>5</sup>European Space Agency, 00044, Frascati, Italy

<sup>6</sup>Research Centre for Atmospheric Physics and Climatology, Academy of Athens, 10680 Athens, Greece

**Correspondence:** Theodoros Christoudias (t.christoudias@cyi.ac.cy)

## Abstract.

Land-atmosphere interactions govern the process of dust emission and transport. An accurate depiction of these physical processes within numerical weather prediction models allows for better estimating the spatial and temporal distribution of the dust burden and the characterisation of source and recipient areas. In the presented study, the ECMWF-IFS (European Centre for Medium-Range Weather Forecast - Integrated Forecasting System) outputs, produced with and without the assimilation of Aeolus quality-assured Rayleigh-clear and Mie-cloudy Horizontal Line of Sight wind profiles, are used as initial/boundary conditions in the Weather Research and Forecasting model coupled with Chemistry (WRF-Chem) to simulate two-month long periods in the spring and autumn of 2020, focusing on a case study in October. The experiments have been performed over the broader Eastern Mediterranean and Middle East (EMME) region that is frequently subjected to dust transport, as it encompasses some of the most active erodible dust sources. Aerosol and dust-related model outputs (extinction coefficient, optical depth and concentrations) are qualitatively and quantitatively evaluated against ground- and satellite-based observations. Ground-based columnar and vertically resolved aerosol optical properties are acquired through AERONET sun photometers and Polly<sup>XT</sup> lidar, while near-surface concentrations are taken from EMEP. Satellite-derived vertical dust and columnar aerosol optical properties are acquired through LIVAS and MIDAS, respectively.

Overall, in cases of either high or low aerosol loadings, the model predictive skill is improved when WRF-Chem simulations are initialised with the meteorological fields of Aeolus wind profiles assimilated by the IFS. The improvement varies in space and time, with the most significant impact observed during the autumn months in the study region. Comparison with observation datasets saw a remarkable improvement in columnar aerosol optical depths, vertically resolved dust mass concentrations and near-surface particulate concentrations in the assimilated run against the control run. Reductions of model biases, either positive or negative, and an increase in the correlation between simulated and observed values were achieved for October 2020.

## 1 Introduction

The Levantine basin and Eastern Mediterranean are frequent recipients of dust transported from North Africa and the Middle East (Gkikas, 2013, 2016), receiving an estimated annual influx of 40-150 g/m<sup>2</sup> (Ben-Asher, 2019). Even though dust deposition can enhance the growth of terrestrial and oceanic ecosystems, high dust loads can have severe implications for human health, increasing the probability of a population developing respiratory and cardiovascular diseases (Kanatani, 2010; Xu, 2019). Additionally, dust storms affect the built environment by degrading the life of electrical equipment, impacting several modes of transport, decreasing the efficiency of solar-harnessing technologies and severely damaging crop output (Hachicha, 2019; Middleton, 2017; Weinzierl, 2012; Stefanski, 2009).

Dust sources are characterised as areas with high availability of alluvium silts and high wind speeds. Some of the most critical Sahelian dust sources include the Bodélé and the Mauritania-Mali locality, with the former being responsible for the production of 6-18% of global dust emissions (Todd, 2007; Engelstaedter, 2007). The combination of various factors, such as moisture content and surface roughness, determine the threshold velocity (Gillette, 1989; Ravi, 2011), which, if exceeded, causes dust to become uplifted. Once suspended, dust from North Africa can reach as far as the Caribbean (Prospero, 1999, 2014) depositing 261±48 Tg along its path (Ridley, 2012). Approximately 30-50% of the dust emitted from the Sahel is transported through the North Atlantic trajectory (Prospero, 1996) during the summer months. Meanwhile, eastward branches transporting dust towards the EMME region peak during late spring and summer (Middleton, 2001). In recent years, an increasing contribution of dust loads in the EMME region from Middle Eastern sources has been highlighted (De-Châtel, 2014; Pozzer, 2015; Notaro, 2015; Kelley, 2015; Logothetis, 2021) and attributed to changing climatic conditions. Specifically, the El-Nino Southern Oscillation and the Pacific Decadal Oscillation teleconnections (Kelley, 2015; Pozzer, 2015) have been linked to a regime shift in dust activity of the Fertile Crescent area in Mesopotamia (Notaro, 2015). Prolonged periods of droughts subsequently decreased soil moisture, where in the work of Klingmüller (2016), an R<sup>2</sup> of 0.82-0.89 was established between decreased soil moisture and the observed positive trend in dust activity for Saudi Arabia and Iraq. Gkikas (2022) identified seasonal variability in the dust optical depth over Mesopotamia, with spring and summer peaks. Dust storms, convective cold pools and nocturnal low-level jets are responsible for 80% of dust transport during late spring and early summer (Heinold, 2013; Chedin, 2018). Anticyclonic activity of synoptic and sub-synoptic scale in the Mediterranean promotes dust transport in the region (Hatzaki, 2014; Ioannidou, 2008). Throughout all seasons, the western North African region is typically the source of the anticyclones, while areas within the East Mediterranean, such as Greece, have been identified as sinks (Lolis, 2014; Trigo, 2004).

The continuous improvements in the computational capability of numerical weather prediction (NWP) models and the growth of available high-resolution observations have significantly improved the accuracy of dust episode forecasting. Numerous sources of uncertainty still prevail, specifically the description of the dust source function and wind fields within an NWP model. Previous work improving the former source of uncertainty has been demonstrated in global models through the works of Ginoux (2001), Zender (2003), Schepanski (2009) and Nabavi (2017), meanwhile Kok (2014) and Wu (2016), have achieved similar improvements by including a threshold velocity parameterisation. However, significant variability in total dust emissions within global models persists, with emissions ranging from 500 to 6000 Tg/yr (Ginoux, 2001; Huneus,

55 2011; Prospero, 2010), attributed to differing model parameterisations and configurations used (Uno, 2006; Huneus, 2011). Alonso-Pérez (2012) and Cavazos-Guerra (2012), assessed the capabilities of dust emission simulations using a Lagrangian-Eulerian model and a regional WRF-Chem (Weather Research and Forecasting model with Chemistry (Grell, 2005)) model, respectively, constrained to West Sahara sources. Both study periods pre-date the recent negative dust trend observed for dust sources of Saharan origin (Mehta, 2016; Chedin, 2018; Shaheen, 2021). Tegen (2013) using the COSMOS (Consortium for  
60 Small scale Modelling) meteorological model for the years 2007 and 2008 for the Sahara region, identified challenges in the model ability to accurately depict inter-annual variability due to gaps in understanding controls of the atmospheric dust load. Nabavi (2016) identified existing challenges of dust source functions within the WRF-Chem model unable to accurately depict dust sources in Mesopotamia, an area of increasing importance in dust studies. Following, Nabavi (2017) tested a new function termed WASF (West Africa source function) within the WRF-Chem model, aiming to improve multi-year analysis for the  
65 summers of 2008–2012. The incorporation of the WASF significantly improved the Spearman correlation, but the accuracy of forecasts dropped with increasing distance from the source, signifying deficiencies in model transport and deposition mechanisms (Nabavi, 2017). More recently, a high-resolution source function was developed by Parajuli (2019) and was able to identify new dust sources, however its use is limited to small-scale studies.

The WRF-Chem model allows the implementation of various parameterisation schemes for dust modelling, with numerous  
70 studies enhancing the model to be particularly suitable for the EMME region (Ukhov, 2020). Tsarpalis (2018) assessed the impact of a deposition scheme using a dust outbreak in June 2014 affecting the Eastern Mediterranean. It was concluded that reductions in overestimations of dust residing at heights greater than 1 km could be achieved. However, underestimations increased at the surface level. Rizza (2018) simulated a dust outbreak in March 2016 at the Central Mediterranean and inter-compared three soil property models. The NoahMP model was performing the best, but in all three runs, the dust peak was  
75 time-shifted relative to the observed peak. Flaounas (2017) studied months of peak activity for the year 2011, with three dust emission parameterisation schemes, highlighting the importance of long-term simulations for sensitivity testing. Compared to the targeted sensitivity testing of the WRF-Chem model performed for the Central and East Asia regions, a gap exists in inter-comparison studies over the EMME region, particularly in assessing individual dust simulation components (Darmenova, 2009; Kang, 2011; Su, 2015; Yuan, 2019; Zeng, 2020; Zhao, 2020).

80 The model predictive ability also benefits from an observational coverage network able to provide the model with observations. Even though there is broad coverage of ground-based stations along the European-Mediterranean border, this does not stand true for the North-African border and the Middle East region. The shortcoming of ground-based observational data can be overcome through the use of ever-increasing satellite products, one being the recently launched Aeolus Doppler wind lidar. The European Space Agency (ESA), in August 2018, launched the Aeolus satellite carrying ALADIN, the first-ever  
85 space-based lidar. ALADIN, via the HSRL (high spectral resolution lidar) technique (Shiple, 1983), acquires horizontal line of sight (HLOS) wind profiles up to 30 km all over the globe. Thus, advancing the current poor observational capabilities, particularly in the open seas of the Southern Hemisphere and the vast desert areas. The first assessment studies (Baars, 2020; Lux, 2020; Witschas, 2020) of Aeolus wind products during the satellite commission phase (autumn 2018) revealed the capability of Aeolus to derive high-quality wind profiles. The main scientific goals of the Aeolus satellite mission are to advance

90 NWP and upgrade the current level of knowledge on atmospheric dynamics and their associated impacts on climate (Stoffelen, 2005; Isaksen, 2019; Rennie, 2019). The positive impact of Aeolus wind data implementation on NWP has been demonstrated by the ECMWF starting the operational assimilation of Aeolus L2B wind data on January 2020 (Baars, 2020). Such activities have also been adopted by other European weather forecast centres (DWD, Météo-France and UK MetOffice). Rennie (2021), demonstrated the beneficial impact of the incorporation of Aeolus wind data on the short- and medium-term forecasts in the S. Hemisphere, in polar regions as well as in latitudinal bands where the well-developed “dust belt” stretches (Prospero, 2002). Since winds trigger dust mobilisation and drive the advection patterns of dust plumes, a subsequent positive impact of Aeolus on numerical dust simulations is anticipated. This improvement constitutes the overarching objective of the NEWTON (ImproviNg dust monitoring and forEcasting through Aeolus Wind daTa assimilation; <https://newton.space.noa.gr/>) project funded by the ESA in the framework of the Aeolus+ Innovation call. In this study, the Aeolus wind fields provided by ESA and assimilated by ECMWF-IFS are implemented in the WRF-Chem to study the effect on the simulated dust. The model is initialised with two sets of IFS outputs that differ only in the inclusion or not of Aeolus wind profiles in the respective assimilation scheme. Four WRF-Chem runs were produced for April - May and September – November 2020, capturing the dust seasons of the EMME region.

This article is structured as follows, in Sects. 2.1 to 2.3 the regional WRF-Chem model setup is described and in Sect. 2.5 the observation datasets and the collocation methodologies undertaken are explained. Sect. 3.1 describes the meteorological conditions simulated using the ECMWF-IFS products with and without Aeolus. Finally, in Sects. 3.2 and 3.3 model outputs are compared against surface measurements provided by AERONET, EMEP and Polly<sup>XT</sup> and satellite-based MIDAS and LIVAS, leading to conclusions in Sect. 4.

## 2 Data and Methodology

110 In the following section, the WRF-Chem regional model configuration and the assimilation of the Aeolus wind fields within the ECMWF-IFS model are discussed in 2.1 and 2.2 respectively. Ground- and satellite-based observation datasets used to evaluate the model are discussed in section 2.5, alongside the methods employed for their spatio-temporal collocation to simulated outputs.

### 2.1 WRF-Chem Model Setup

115 The WRF-Chem version 3.9.1.1 was used along with the WRF Pre-Processing System version 4.2 to perform meteorological and air quality simulations adjusted for the study region as described below.

The Regional Atmospheric Chemistry Mechanism (RACM) was applied to simulate gas-phase chemistry. RACM is based on the Regional Acid Deposition Model, version 2 mechanism and has been shown by Georgiou (2018) that it produces the lowest mean bias for hourly concentrations of fine particles over the region of interest compared to other gas-phase chemistry mechanisms. The Modal Aerosol Dynamics Model for Europe (MADE) and the secondary organic aerosol (SOA) parameterisation based on the volatility basis set by Ahmadov (2012) were employed to simulate aerosol inorganic species and SOA, respec-

tively. Anthropogenic emissions were based on the Emission Database for Global Atmospheric Research for Hemispheric Transport of Air Pollution (EDGAR-HTAP) Version 5 emission inventory compiled by the European Commission, Joint Research Centre/Netherlands Environmental Assessment Agency (Janssens-Maenhout, 2012). The Model of Emissions of Gases and Aerosols from Nature version 2.1 (MEGAN2.1) by Guenther (2012) was employed to generate biogenic emissions based on weather and land use data.

Mineral dust and sea-salt emissions were calculated on-line by the WRF-Chem model, driven by IFS Aeolus-assimilated data. The Georgia Tech/Goddard Global Ozone Chemistry Aerosol Radiation and Transport (GOCART) model (Ginoux, 2001), coupled with the MADE/SORGAM aerosol mechanism within the framework of WRF-Chem, was used to simulate dust emission. The dust emission flux in the GOCART model is scaled by an empirical proportionality constant  $C$ . The value of  $C$ , estimated by Ginoux (2001), was initially based on US regional data. Zhao (2010) evaluated the performance of the WRF-Chem model for different values of  $C$ . They found that for  $C = 0.4 \mu\text{gs}^2/\text{m}^5$ , the WRF-Chem simulated mean aerosol optical depth (AOD) was consistent with the AERONET measurements at two sites over the Sahel region and aerosol size over North Africa (Zhao, 2010). Several sensitivity tests performed over Cyprus and the East Mediterranean led to the best performing value of  $0.36 \mu\text{gs}^2/\text{m}^5$  (Georgiou, 2018), based on the study of modelling sensitivities to dust emissions. Therefore, as this is the most prevalent source of dust emissions in the EMME region, in the following simulations, a value of  $C$  equal to  $0.36 \mu\text{gs}^2/\text{m}^5$  was used. The radiation scheme Rapid Radiative Transfer Model (RRTMG) has been used due to the incorporation of a two-stream radiative transfer solver (Oreopoulos, 1999) that enables a more accurate calculation of extinction from aerosols in the presence of multiple scattering (Iacono, 2008), compared to other schemes. A summary of the model configuration options is presented in Table A1 of the Supplement.

## 2.2 Aeolus assimilation

The WRF numerical experiments are performed using the simulated meteorological fields from the IFS as initial and boundary conditions. The IFS refers to a global numerical weather prediction system of the ECMWF. Two sets of outputs were produced by IFS, a control and an experimental run. Both IFS outputs have a 6-hour temporal resolution and are projected on an equal lat-lon grid at  $12 \times 12$  km spatial resolution. The configuration of the IFS runs is thoroughly described in Rennie (2021) (see the second row in Table 1). The experimental run includes the Aeolus L2B (2B10 baseline, from 28 June to 31 December 2019 and from 20 April to 8 October 2020) Rayleigh-clear and Mie-cloudy HLOS wind profiles (Baars, 2020; Rennie, 2019). Aeolus HLOS retrievals are subjected to a quality screening identical to the one applied in the Observing System Experiments, detailed in the work of Rennie (2021). Both simulations assimilate observations to reproduce the optimum state of the atmosphere (i.e., analysis). For the analyses at 00 UTC and 12 UTC, observations falling within the time windows spanning from 21 UTC (the day before) to 09 UTC and from 09 UTC to 21 UTC, respectively, are assimilated. The assimilation is done with the 4D-Var technique via a process called LWDA (Long Window Data Analysis; formerly known as “delayed cut-off”, Haseler (2004)), which allows the maximum use of all observations falling within the assimilation time window. Short-term forecasts are initialised at the start of the time window (either 21 UTC or 09 UTC), which correspond to the analysis fields at 00 UTC and 12 UTC and to intermediate nominal model times (i.e., 06 UTC and 18 UTC).

The analyses IFS numerical outputs serve as initial/boundary conditions in the WRF-Chem model and are exactly the same as those described in Rennie (2021) (Section 2.3: Observing system experiments). The WRF-Chem simulations using the IFS outputs were contrasted to investigate the modifications in the meteorological patterns and the subsequent variations in the simulated dust fields.

## 160 2.3 Experiments set-up

The WRF-Chem model was used to simulate the periods 2020/04/04 - 2020/05/31 and 2020/09/01 - 2020/11/04 using boundary conditions with (assimilated), and without (control) IFS Aeolus assimilated data. The periods under investigation coincide with the dust storm high-activity phase of the East Mediterranean (Engelstaedter, 2006; Miller, 2008; Tyrllis, 2014). The domain area has been configured to a horizontal grid resolution of 20 x 20 km, extending from 5° to 45° in latitude and -20° to 62.5°  
165 in longitude, spanning over the three primary dust sources affecting the region (domain area visualised in Fig. A1). Including the Saharan, Syrian and Arabian deserts in the model domain allows to not require the dust component from the boundary conditions and helps avoid biases in dust concentrations from global models. The WRF-Chem model uses a terrain-following hydrostatic-pressure vertical coordinate system. The model configuration uses 30 layers, from the surface up to 50 hPa, with an average height of 70 m for the first layer.

170 The WRF-Chem model has Four-Dimensional Data Assimilation (FDDA) capabilities, described in Deng (2012). FDDA has been applied towards IFS re-analysis fields with and without assimilated Aeolus observations. It was shown that by nudging above and within the Planetary Boundary Layer, the accuracy of the meteorological variables simulated within the WRF-Chem model is improved (Deng, 2007) and has since been used in other dust-related studies (e.g. Kumar (2014)). Following this, the horizontal wind components, temperature and moisture were nudged in all the model vertical layers, except the surface level,  
175 with a nudging coefficient of  $3 \times 10^{-4} \text{ s}^{-1}$ . Nudging was carried out at each time step throughout the whole simulation, with a time interval between analysis times of 6 hours. Ramping started at the last analysis time and ended as a step function.

To evaluate the performance of WRF-Chem with the introduction of the ECMWF-IFS dataset, we employ the atmospheric extinction coefficient variable at the wavelength of 550 nm (EC55). EC55 profiles get computed through the radiation scheme RRTMG and can be integrated to produce the total aerosol optical depth. For the AOD calculation, dust particles are assumed  
180 to be spherical and internally mixed in five differing-size bins of an effective particle radius of 0.5, 1.4, 2.4, 4.5 and 8.0  $\mu\text{m}$ . The Mie theory has been used to calculate the optical properties as a function of wavelength at each model grid point for the wavelengths of 300, 400, 600 and 999 nm as described in Barnard (2010). More specifically, the aerosol optical thickness, the single scattering albedo and the asymmetry parameter were determined by interpolation at the wavelength of the centre of the band located between the four wavelengths (Chaibou, 2020).

## 185 2.4 FLEXPART

For the characterisation of the origins of air masses, the Lagrangian particle dispersion model FLEXPART (Stohl, 2005; Brioude, 2013; Pisso, 2019) was run in a backward mode for the period 14th to 25th October 2020. The backward FLEXPART-WRF runs were performed by releasing 10,000 tracer particles at heights 0.5, 1, 2, 3, 4, 5, 7 and 10 km over the Agia Marina,

Cyprus station. The FLEXPART simulations were driven by hourly meteorological fields from the WRF-Chem model initiated  
190 with control and assimilated datasets.

## 2.5 Observation Datasets

To evaluate the performance of the WRF-Chem model, ground-based AERONET AOD, EMEP coarse particulate matter  
(PM10) and Polly<sup>XT</sup> vertical dust concentrations were used. These were accompanied by space-borne horizontal and verti-  
195 cal dust products from MIDAS and LIVAS, respectively. Spatial and temporal collocations were applied to enable a direct  
comparison between simulated and observed variables, which are discussed in the following sub-sections.

### 2.5.1 AERONET

AERONET (AERonet RObotic NETwork) is a global network of about 1000 ground-based monitoring instruments distributed  
globally and maintained by NASA (Holben, 1998). The sunphotometer instruments measure the spectral AOD (a unitless  
measure of aerosol load throughout the total atmospheric column), aerosol size parameters (e.g., Ångström exponent) and  
200 several other optical and microphysical properties (Dubovik, 2000, 2006). Due to the limited availability of Level 2, cloud-  
screened and quality-assured data, Level 1.5 (only cloud-screened) AOD measurements (Version 3, (Giles, 2019; Sinyuk,  
2020)) are taken from 56 stations located within the WRF-Chem constructed domain (location of stations seen on Fig. A4).

The WRF-Chem model does not directly output the AOD and thus has to be calculated using Equations 1 and 2. Where  
 $H_{(t, V, lat, lon)}$  refers to height (km) of the model level,  $\Delta H_{(t, V, lat, lon)}$  to the thickness between model levels,  $EC55_{(t, V, lat, lon)}$  to  
205 the atmospheric extinction coefficient at 550 nm ( $\text{km}^{-1}$ ),  $PH_{(t, V, lat, lon)}$  to perturbation geopotential ( $\text{m}^2/\text{s}^2$ ),  $PHB_{(t, V, lat, lon)}$  to  
base-state geopotential ( $\text{m}^2/\text{s}^2$ ),  $V$  to the vertical layer,  $t$  to the time interval,  $lat$  to latitude and  $lon$  to longitude coordinates. The  
resulting AOD refers to the wavelength at 550 nm. AERONET AOD retrievals at this wavelength are not readily available. To  
make results comparable, AERONET  $AOD_{870}$  has been converted to  $AOD_{550}$  using the Ångström Exponent equation and the  
Ångström exponent of wavelength 440-870 nm (Ångström, 1929). A statistical comparison of  $AOD_{550}$  produced from various  
210 wavelengths was carried out, revealing negligible statistical differences regardless of the wavelength used in the conversion,  
also highlighted in the work of Eck (1999).

$$H = \frac{PH_{(t, V, lat, lon)} + PHB_{(t, V, lat, lon)}}{9.81 * 1000} \quad (1)$$

$$AOD_{t, lat, lon} = \sum_{V=1}^{30} EC55_{(t, V, lat, lon)} * \Delta H_{(t, V, lat, lon)} \quad (2)$$

WRF-Chem outputs variables in regular (hourly) time intervals, while AERONET keeps records in non-constant interval  
215 steps. To temporally collocate the values, observations falling within a  $\pm 30$ -minute range, centred at the model forecast hour,  
are averaged out. A spatial collocation is then implemented to modelled outputs of horizontal resolution 20 x 20 km. Modelled

outputs are interpolated from a three-dimensional field to a horizontal plane at the station's height using the approach described in Ladwig (2017). In summary, the data are interpolated from a curvilinear grid to an unstructured grid using the nearest grid point to the station's coordinates. This approach has been repeated using the four and nine neighbouring grid points with  
220 no statistically significant differences. Finally, an inverse distance squared algorithm is applied to output the variables at the coordinates and elevation of each station.

### 2.5.2 EMEP

The EMEP (European Monitoring and Evaluation Programme) is a pan-European database of ground-based aerosol concentration observations. EMEP was established following the convention of Long-range Transboundary Air Pollution in 1979.  
225 European member states are legally bound to monitor and report emissions to EMEP with a standard temporal resolution of daily intervals. These are then stored in the EMEP open access database and are mapped using a  $0.1^\circ \times 0.1^\circ$  longitude-latitude grid (Pinterits, 2021).

To compensate for the poor temporal and spatial resolution of the EMEP database for the period under investigation, hourly products of PM<sub>10</sub> at the EMEP background station of Agia Marina, Cyprus, were provided by the Department of Labour  
230 Inspection Cyprus (DLI) (Labour Inspection, 2021). For the comparison of observed PM<sub>10</sub> with simulated values, a spatial collocation was carried out in a similar manner to the one described in section 2.5.1. Since both simulated and observed values are reported at hourly intervals, no temporal collocation was required.

### 2.5.3 Polly<sup>XT</sup>

The Polly<sup>XT</sup> lidar monitors the vertical profiles of dust concentrations at the PANGAEA observatory at Antikythera, Greece  
235 (Marinou, 2017). The products are obtained through the application of the Earlinet SCC algorithm described in D'Amico (2015) and in the methodology presented by Mamouri (2017), and Ansmann (2019). The products are only available during cloud-free conditions. It is noted that the calculated dust mass concentrations have an uncertainty of 20-30% for a predominantly dust-dominated layer (Ansmann, 2019), while the uncertainty increases for a moderately dust-dominated layer and can reach up to 100% in layers with a small contribution of dust particles (Marinou, 2019).

The Polly<sup>XT</sup> products were subjected to a spatio-temporal collocation to enable a direct comparison with the simulated data.  
240 Observations are derived from 642 m up to 14 km above sea level, with a 60 m vertical resolution. For the vertical collocation of the two datasets, the Polly<sup>XT</sup> products were averaged for each model vertical bins to match the vertical resolution of the WRF-Chem model. Meanwhile, the same methodology described in section 2.5.1 has been used for the horizontal collocation. Polly<sup>XT</sup> products are derived in temporal averages between 30-minutes and 2-hours depending on weather limitations. Hence  
245 for the temporal collocation, model hourly products were averaged to the Polly<sup>XT</sup> time windows.



## 2.5.4 MIDAS

For evaluating the WRF AOD spatial patterns, the recently developed MIDAS dataset (Gkikas, 2021, 2022) has been utilised as a reference. MIDAS provides columnar mid-visible (at 550 nm) dust optical depth (DOD) derived through the combination of quality-assured MODIS-Aqua AOD retrievals and the portion of AOD attributed to DOD (MDF; MERRA-2 dust fraction) extracted from MERRA-2 (Modern-Era Retrospective analysis for Research and Applications version 2; (Gelaro, 2017; Randles, 2017)). Within MIDAS, the quality assured MODIS-Aqua AOD, as well as DOD (along with its associated uncertainties), are provided at a fine spatial resolution ( $0.1^\circ \times 0.1^\circ$ ) and at a global scale (both over land and maritime surfaces). Since the current WRF model version does not output DOD, the evaluation is focused only on the AOD simulated fields, mainly driven by the spatiotemporal variations of the intense dust loads, spreading within the region of interest and dominating other aerosol species.

In order to achieve the optimum MIDAS-WRF collocation, we are processing the swath level MIDAS data, where for the constructed domain, MIDAS has approximately 5 to 7 daily overpasses corresponding to 5-minutes segments (Levy, 2013). The segments have been reprojected from their native grid (Hubanks, 2018) to an equal latitude-longitude grid at  $0.1^\circ \times 0.1^\circ$  spatial resolution. After conducting several sensitivity tests, the MIDAS dataset was regrided to  $0.4^\circ$  to minimise the noise effect noted when weak loads of AOD are recorded. In contrast to MIDAS, WRF AOD is mapped on an equidistant,  $20 \times 20$  km, Lambert conformal conic projection. To project MIDAS and WRF-Chem AOD on a common grid, both have been regrided on an equal latitude-longitude grid at  $0.4^\circ$  spatial resolution. Regridding was carried out using the nearest neighbour method with a search radius around each grid pixel set at 20 km. The radius was tested with values ranging from 10 to 50 km, resulting in percentage difference ranges of 0.008% - 0.04% and 0.0007% - 0.003% for MIDAS and WRF outputs, respectively. The availability of MIDAS observations depends on the clouds' presence and deterring reasons for retrieving MODIS AOD. This leads to sparse AOD grid values compared to the WRF continuous domain coverage. Thus, a mask function is applied on WRF in the areas where MIDAS failed to resolve a value for AOD and simultaneously temporally collocates the two datasets. For the temporal collocation, three methods have been tested: a 3-hour rolling average, a weighted average and use of the nearest hour. The relative difference between the latter and the former two approaches indicated poor performance and was hence discarded. Meanwhile, a comparison between the two remaining methods revealed negligible statistical differences. The weighted average method has been used to compute the collocation following Eq. 3, where  $AOD_i$  refers to the AOD at the nearest hour,  $AOD_{i+1}$  to the AOD for the hour ahead and  $min$  to the minute of the MIDAS overpass. The hourly outputs have then been summed to produce daily AOD maps. The edges of the overpasses have a slight overlap; to overcome this, values at the overlaps were averaged. Finally, the daily sum maps were averaged to produce a single map for the whole period under investigation.

$$AOD = AOD_{i+1} * \frac{min}{60} + AOD_i * (1 - \frac{min}{60}) \quad (3)$$

### 2.5.5 LIVAS

For the vertical assessment of the simulated dust patterns in the broader study region, the LIVAS (Lidar climatology of Vertical Aerosol Structure for space-based lidar simulation studies) pure-dust product, initially presented in Amiridis (2013) and updated in Marinou (2017), was utilised. LIVAS comprises a global dataset covering the period between 06/2006 and 12/2020 and is provided on per-granule, level 2 resolution similar to the original CALIPSO (Cloud-Aerosol Lidar and Infrared Pathfinder Satellite Observations) level 2 profile products.

The pure-dust extinction coefficient product has been developed through the application of the depolarisation-based separation method introduced by Sugimoto (2003) and Shimizu (2004) and optimised for the Saharan region by Tesche (2009). Marinou (2017) has calculated the uncertainty of the product in the region under investigation to be less than 20% for altitudes up to 6 km. The products have a fine vertical resolution of 60 m and are projected on a uniform grid of  $1^\circ \times 1^\circ$  horizontal resolution. To make observations directly comparable to simulated values, the WRF horizontal grid has been regridded to a  $1^\circ \times 1^\circ$  lat-lon grid and vertically collocated following the methodology described in section 2.5.3.

## 3 Results and Discussion

In section 3.1, the WRF-Chem model runs for spring and autumn are compared, and the meteorological conditions and the subsequent effects on dust transport for the selected study period are discussed. In sections, 3.2 and 3.3, comparisons of assimilated and control outputs to ground- and satellite-based observations are summarised.

### 3.1 Seasonal Patterns and Dust Outbreak in October 2020

The WRF-Chem model, using both control and assimilated Aeolus ECMWF-IFS datasets, was run for two months in spring and two in autumn. Fig. 1, depicting the differences (assimilated - control) of the averaged dust concentrations and wind vectors at the atmospheric level of 850 mb, reveals that the use of the assimilated dataset has negligible differences to the control one during the spring months (1a), while a difference is observed for autumn (1b). During the spring months, the differences in dust concentration between the two model runs are less than  $20 \mu\text{g}/\text{m}^3$  for most of the study region. Meanwhile, for autumn, the differences are more pronounced. A dipole seems to prevail, with the control run having higher concentrations over the Central Mediterranean and the assimilated run over the Eastern Mediterranean, especially true for October. Additionally, a comparison of the two model runs using PM10 from the EMEP station of Agia Marina, Cyprus (Fig. A2 of the Supplement) for spring supports the finding of a small deviation between the two model runs observed for spring. This finding suggests that the impact of the assimilated dataset has temporal (seasonal) variation for the region under investigation, which should be confirmed from long-term runs.

## Comparison of model runs for spring and autumn

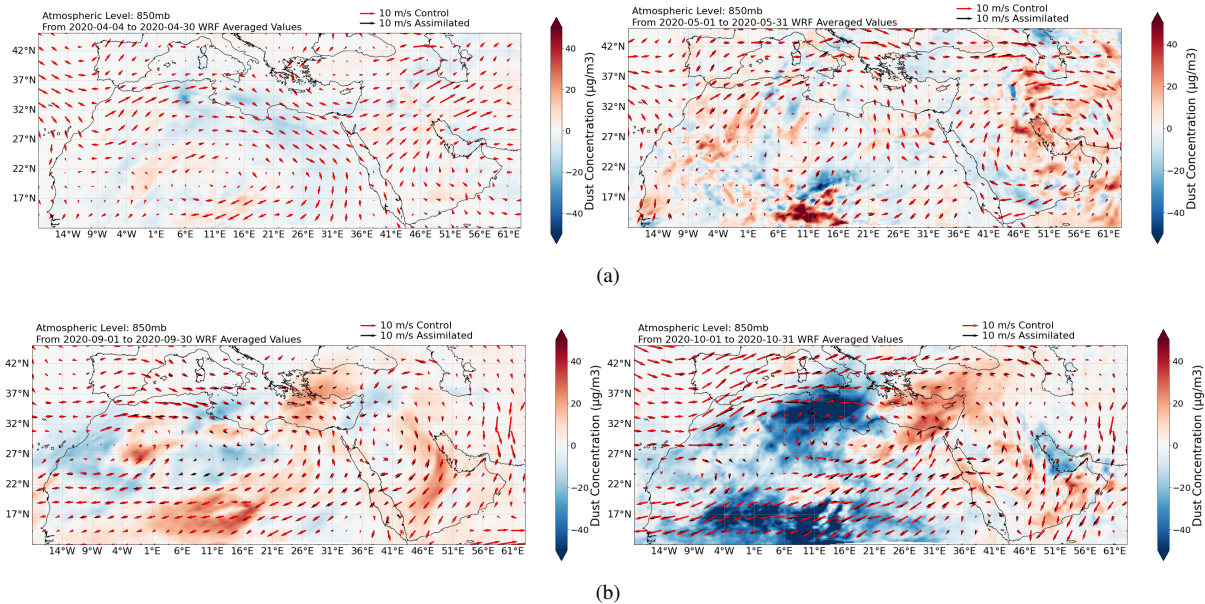


**Figure 1.** Depiction of the difference in monthly average dust concentration and of wind vectors between the assimilated and control datasets, averaged for spring months (1a, April (left), May (right)) and autumn months (1b, September (left), October (right)) for the atmospheric pressure level of 850 mb, where the red arrows represent the control wind vectors and the black arrows the assimilated ones.

305 The availability of surface PM<sub>10</sub> observations at the Agia Marina, Cyprus station, allowed for an initial assessment of the two runs for autumn. Depicted in Fig. 2, two instances, highlighted in blue, mark periods where the assimilated run outperforms the control run, while one instance, highlighted in red, depicts the opposite. Summarised in Table 1 is the statistical analysis for the autumn period, as well as for the three highlighted instances, where counts refer to the number of data points within each timeframe,  $r$  stands for the correlation coefficient and IOA for the Index of Agreement. The IOA measures the closeness of magnitude between two variables and is a unitless metric of range from 0 to 1, where 1 indicates perfect agreement (following equation 5 in Willmott (2011)).

310 During most of the period, minor differences are recorded between the two runs. However, the assimilated run performs slightly better than the control, with the highest improvement observed for the interval of 20-25<sup>th</sup> of October. It is noted that the total sample size is small to draw statistically significant conclusions. The period 14-25<sup>th</sup> of October 2020 was selected due to the formation of a dust storm of anticyclonic nature affecting the modelled domain,

315 with notable deviations between the two model runs. The selected period allows for an investigation of the impact of ECMWF-IFS Aeolus on meteorology, hence dust mobilisation.

## EMEP Timeseries for PM10 at Agia Marina, Cyprus, station for autumn

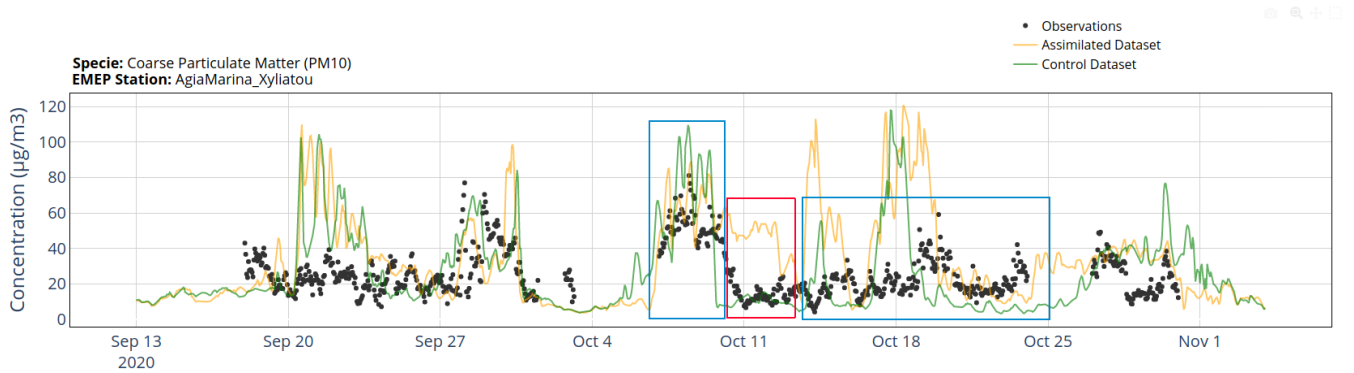


**Figure 2.** Timeseries of PM10 concentrations recorded at Agia Marina, Cyprus, ground station for the months of autumn, where the green represents the control run, the yellow the assimilated run and the black dots the observed values. Additionally, the blue highlighted boxes represent periods where the assimilated run outperforms the control run, while the red box represents the opposite.

**Table 1.** Statistical comparison of modelled runs with PM10 concentrations recorded at Agia Marina station, Cyprus, for the whole period and the highlighted time windows.

Periods	Whole Period		07/10/2020 - 10/10/2020		11/10/2020 - 14/10/2020		14/10/2020 - 25/10/2020	
Counts	952 (100%)		46 (4.8%)		94 (9.8%)		146 (15.3%)	
Dataset	Control	Assimilated	Control	Assimilated	Control	Assimilated	Control	Assimilated
r	0.31	0.33	0.37	0.43	-0.53	0.11	-0.12	0.28
IOA	0.51	0.52	0.42	0.58	0.28	0.27	0.22	0.34

In the study of Hatzaki (2014), two major anticyclonic routes were identified, one parallel to the Iberian Peninsula and another parallel to the North African Coast, with the latter being the dominant route during summer and autumn. Consistent with past literature, during the 14-19<sup>th</sup> of October, a high-pressure cell developed in both simulations covering the Levantine basin and extending to North Africa, as seen in Fig. 3. The high-pressure conditions ushered clockwise wind motion forming an anticyclone just north of the great sand sea desert in the Sahara region, 30° N and 25° E. The warm-core anticyclone developed from the convergence of the upper troposphere leading to air subsidence and warmer temperatures (Musk, 1988). The anticyclone developed near the 30° N line, consistent with past literature findings of warm-core anticyclonic development in the subtropics and midlatitude regions (Flocas, 2001; Hatzaki, 2014).

The anticyclogenesis on the 14-19<sup>th</sup> of October mobilised and transported dust through the gulf of Sidra into the Mediterranean basin. The two models have near-identical pressure zones for this period (Figs. 3a and 3b). However, the minor deviations led to dust transported North-East in the assimilated run with increased dust concentration on the west sector of the anticyclone, while South-West in the control run with higher dust concentration over Egypt, as depicted in Fig. 4a. This can be attributed to the extension of the high-pressure cell North-West of Cyprus in the assimilated run, driving winds towards the

330 Dodecanese and Anatolia. In contrast, the weaker high-pressure cell in the control run led to dust transport southwards from the Levantine basin to Egypt. During the 20-25<sup>th</sup>, the high-pressure system moved westwards. In the control run, it remained more defined (Fig. 3c), while in the assimilated run, it weakened and dissipated (Fig. 3d). A second anticyclone formed in the control run with its focal point just off the coast of Tunisia indicated in Fig. 4b and also observed in terms of absolute vorticity (see Fig. A3 of the Supplement). The anticyclonic motion is not pronounced in the assimilated run, leading to markedly lower  
335 dust concentrations over the Central Mediterranean and higher values over Egypt and the Middle East. The higher concentrations can be attributed to the more stagnant conditions in the Eastern Mediterranean, where clockwise wind motion around 30° N 40° E mobilised dust from the Arabian desert towards the Red Sea and the Levantine basin. The anticyclonic motion modelled in the control run led to higher wind speeds over the Central Mediterranean and Libya, while north-easterly winds passed through the Levantine basin (Fig. A3a of the Supplement). Meanwhile, in the assimilated run, lower wind speeds were  
340 simulated over the Levantine and Central Mediterranean basins, as well as on the coastline of North Africa (Fig A3b of the Supplement).

Additionally, four FLEXPART-WRF air mass back-trajectories were simulated for a total of two 5-day periods (14-19<sup>th</sup> and 20-25<sup>th</sup>), with particles arriving at the Antikythera, Greece station and the Agia Marina, Cyprus station. Similar air-mass routes were noted for both stations with results being more notable for particles arriving at the Agia Marina station on the 19<sup>th</sup> of  
345 October. Fig. 5 reveals apparent differences in the vertical height and source regions of aerosols arriving at the Agia Marina, Cyprus station, on the 19th of October at 02:00 UTC. The assimilated run simulated the arrival of aerosols from North African dust sources, while in the control run, aerosols originated from continental Europe.

## Pressure gradient of model runs for the 14-25<sup>th</sup> of October 2020

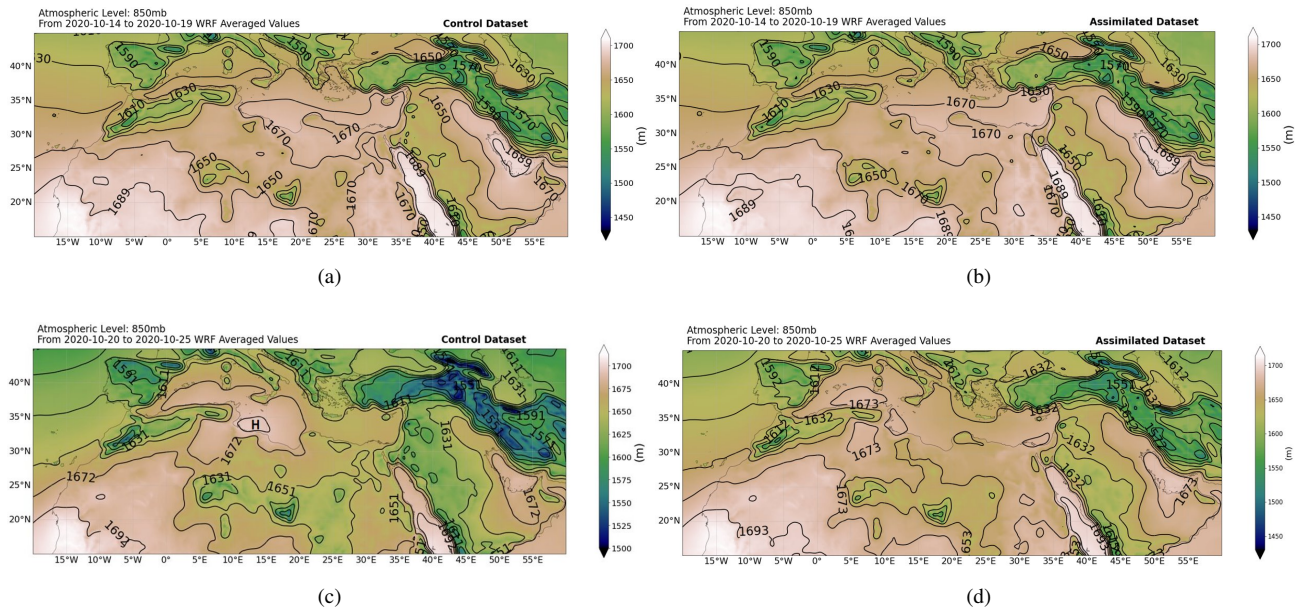


**Figure 3.** Representation of the averaged geopotential height for the 14-19<sup>th</sup> of October in the control run (3a) and assimilated run (3b) and for the 20-25<sup>th</sup> of October in the control run (3c) and assimilated run (3d) for the atmospheric layer at 850 mb.

## Dust Concentration Differences between the model runs for the 14-25<sup>th</sup> of October 2020

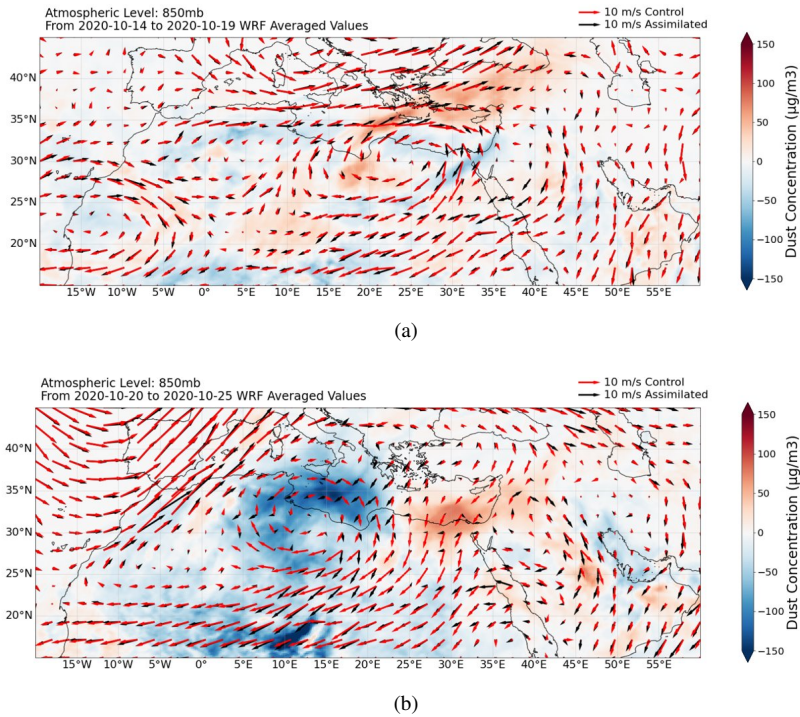


**Figure 4.** Averaged dust concentration differences (assimilated - control) and wind fields at the atmospheric level of 850 mb for the time-averaged periods; 14-19 of October (4a) and 20-25 of October (4b) where the red arrows represent the control wind vectors and the black arrows the assimilated ones.

## FLEXPART backward trajectories for the 19<sup>th</sup> of October 2020 at Agia Marina Cyprus

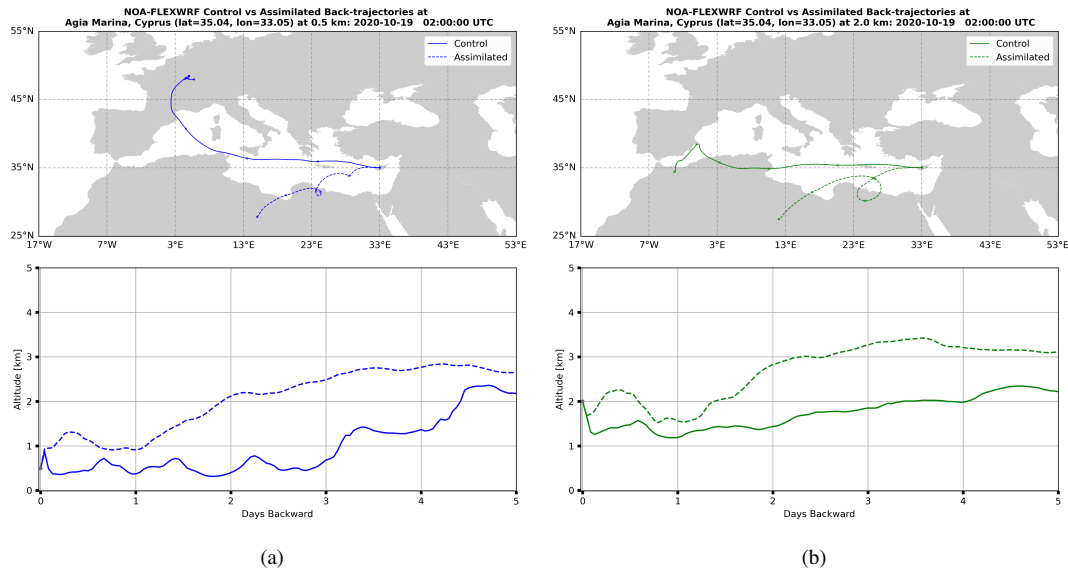


**Figure 5.** The top panel figures depict the FLEXPART backward trajectories for tracer particles arriving at the Agia Marina, Cyprus station at 0.5 km (5a) and at 2 km (5b) on the 19<sup>th</sup> of October at 02:00 UTC. A solid line represents the trajectory of the control run, and a dashed line of the assimilated run. Additionally, the altitude inclinations of the particles are depicted in the bottom panel figures.

### 3.2 Ground-Based Evaluation

For the horizontal, spatio-temporal evaluation of the model runs, AOD from 56 AERONET sun-photometers within the whole  
350 extended domain have been sourced. The map of stations used can be found in Fig. A4 of the Supplement. For the vertical evaluation of dust concentration, the Polly<sup>XT</sup> lidar at Antikythera station in Greece has been used.

The simulated high dust concentration over the Central and East Mediterranean on the 14<sup>th</sup> to the 25<sup>th</sup> of October (Fig. 4) led to the assumption of a dust-dominated AOD, also supported by FLEXPART trajectories (Fig. 5). In the study of Formenti (2001), the Mediterranean basin was characterised as a hotspot of long-range transport of tropospheric trace gases and aerosols.  
355 With base values 2 to 10 times higher than the hemispheric background troposphere (Lelieveld, 2002). The pressure gradient between the Azores high and Asian monsoon causes an eastward influx of small-sized particles in the EMME region (Lelieveld, 2002). To identify dust-dominated loads of AERONET total atmospheric column retrievals, a filter on AOD and Ångström exponent was applied. In previous AOD studies in the EMME region, the cut-off thresholds for AOD and Ångström indicating a dust-dominated AOD have been placed within the ranges of  $> 0.15$ - $0.35$  and  $< 0.40$ - $0.75$  respectively (Fotiadi, 2006; Basart,  
360 2009; Toledano, 2007). The threshold of Ångström exponent  $< 0.75$  has been selected following the study of Gkikas (2021), which found this threshold to be well performing in capturing coarse particles. Additionally, a cut-off level of AOD  $> 0.15$  has been used to minimise the contribution from coarse sea-salt aerosols (Gkikas, 2021). Thereby, values that satisfy these conditions were classed as dust-dominated and were used in the statistical analysis summarised in Table 2. It is noted that the



unfiltered AOD readings, accompanied by the Ångström exponent values, are used in the time-series plots (Fig. 6), showcasing all available observations.

A statistical improvement is obtained for all 56 AERONET stations when implementing the Aeolus wind dataset, which is stronger for stations located in the Central Mediterranean and EMME regions (stations highlighted in fig. A4). Metrics were produced for selected stations impacted by the anticyclogenesis mentioned above (14-25<sup>th</sup>), as well as for the two smaller time windows (14-19 and 20-25). This was done to test whether the improvement arises due to the materialisation of an anticyclone only in the control run from the 20<sup>th</sup> onwards (see 3.1). For both periods and the whole period, an improvement of 0.20-0.22 in the correlation coefficient is obtained using the assimilated dataset. This indicates that the improvement is not solely attained from an isolated instance. The anticyclonic conditions that prevail in the control run for the period of 20-25<sup>th</sup> of October 2020 over the Central Mediterranean are the underlying reason for the higher AOD profiles modelled at the impacted stations of; Lampedusa and Lecce University in Italy, Gozo in Malta and Finokalia and Antikythera in Greece. Meanwhile, the more stagnant wind conditions simulated in the assimilated run produced lower AOD values atop these stations and are more coherent to observations, as depicted in Fig 6. During this period, the assimilated run computes higher dust concentrations in the Levantine basin translating to a high AOD, consistent with a high AERONET AOD and low Ångström exponent recorded at Agia Marina and CUT-TEPAK, Cyprus stations, as well as Tel-Aviv University and Sede Boker stations in Israel. The locations of the stations mentioned can be found in Fig. A4 of the supplement

**Table 2.** Statistical comparison of filtered AERONET AOD observations to model outputs for all 56 AERONET stations and for selected stations for the 14-25<sup>th</sup> of October 2020.

	<b>All Stations 14-25/10/2020</b>		<b>Selected Stations 14-25/10/2020</b>		<b>Selected Stations 14-19/10/2020</b>		<b>Selected Stations 20-25/10/2020</b>	
<b>Datasets</b>	Control	Assimilated	Control	Assimilated	Control	Assimilated	Control	Assimilated
<b>Counts</b>	4835 (100%)		437 (9.0%)		212 (4.4%)		263 (5.2%)	
<b>r</b>	0.46	0.51	0.12	0.33	0.23	0.43	0.22	0.44
<b>IOA</b>	0.41	0.45	0.38	0.52	0.48	0.59	0.37	0.52

## Model evaluation through AERONET AOD, October 2020

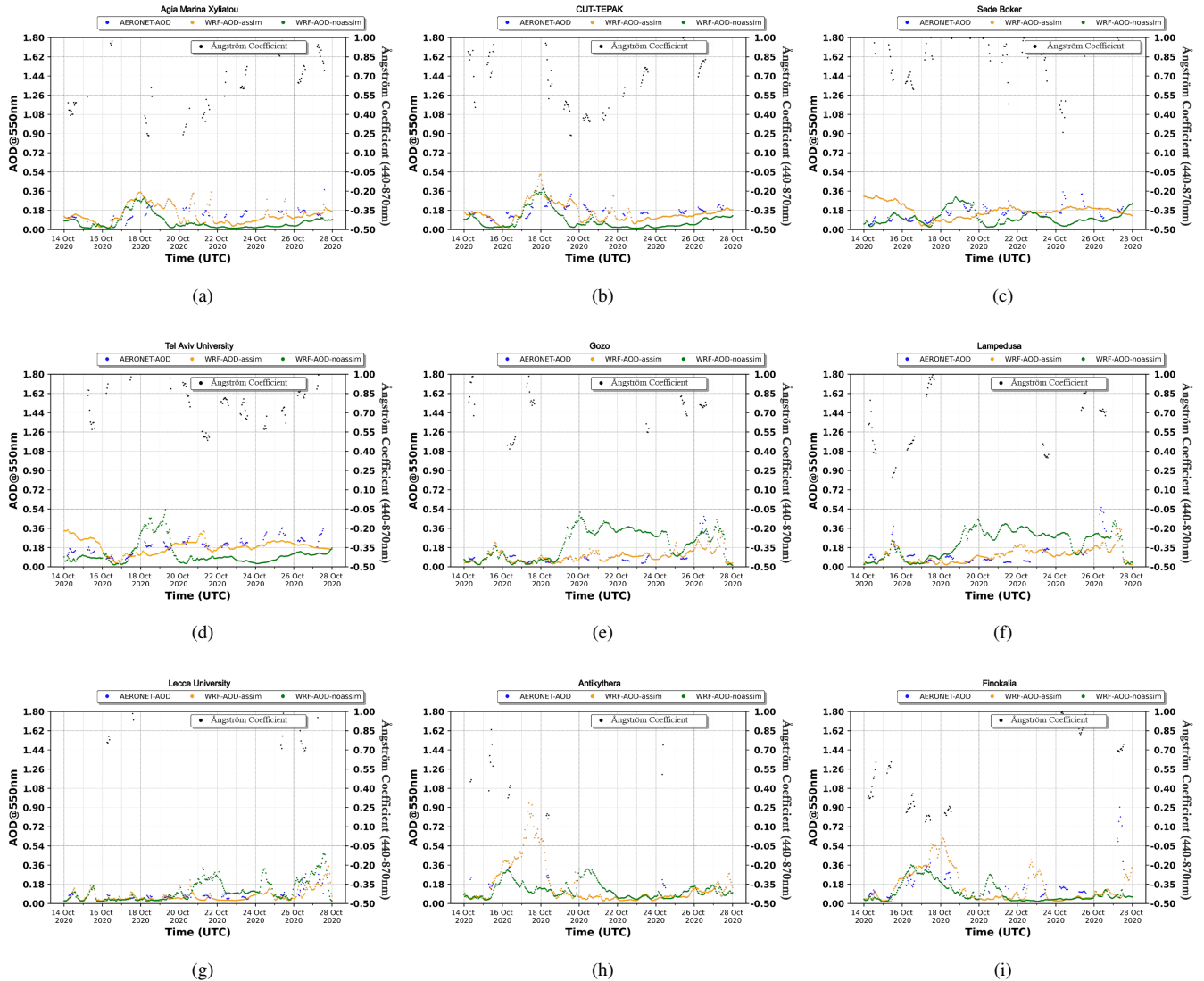


**Figure 6.** Timeseries plots of observed AOD (blue points) from AERONET stations within the model domain, contrasted against assimilated AOD (yellow) and control AOD (green). Additionally, the black points represent the Ångström Coefficient obtained from the AERONET stations.

380 To supplement AERONET observations, the vertical dust profile at Antikythera station was obtained through the Polly<sup>XT</sup> lidar, depicted in Fig 7. In the works of Papayannis (2005), Mona (2006) and Kalivitis (2007), the highest dust concentrations in the Mediterranean during autumn were observed at 2-5 km, consistent with Polly<sup>XT</sup> observations, while both model runs display the highest dust concentrations from 1-4 km. During the 15-19<sup>th</sup> of October, the assimilated run overestimates while the control run underestimates dust concentrations, with the former having a better fit to the observed vertical structure. The

385 over/under estimation could be explained by the 20-30% uncertainty of the lidar products (Ansmann, 2019). The formation  
of an anticyclone in the control run is materialised as a dust plume over Antikythera, arriving on the 20<sup>th</sup> and dispersing by  
the 22<sup>nd</sup> (Fig. 7a). In contrast, the assimilated run did not simulate the dust plume and is in better agreement with the limited  
observations available from Polly<sup>XT</sup> and the complementary observations from MIDAS and SEVIRI as shown in Figs. A5 and  
A6. Where for MIDAS, AOD values less than 0.3 are recorded in the area and from the SEVIRI natural enhanced imagery and  
390 dust RGB composites, no dust plume is resolved in the area (see Figs. A5 and A6 of the Supplement). During the 23-25<sup>th</sup>, the  
assimilated run simulates the arrival of a dust plume earlier than observed but has a more consistent vertical structure relative  
to the control run.

Overall, these results support that when implementing the assimilated dataset, the predictive ability of the WRF-Chem model  
for the specified regions is improved. This is perhaps related to the volatile conditions present in the Mediterranean during the  
395 transitional autumn season.

## Model evaluation using Polly<sup>XT</sup>, October 2020

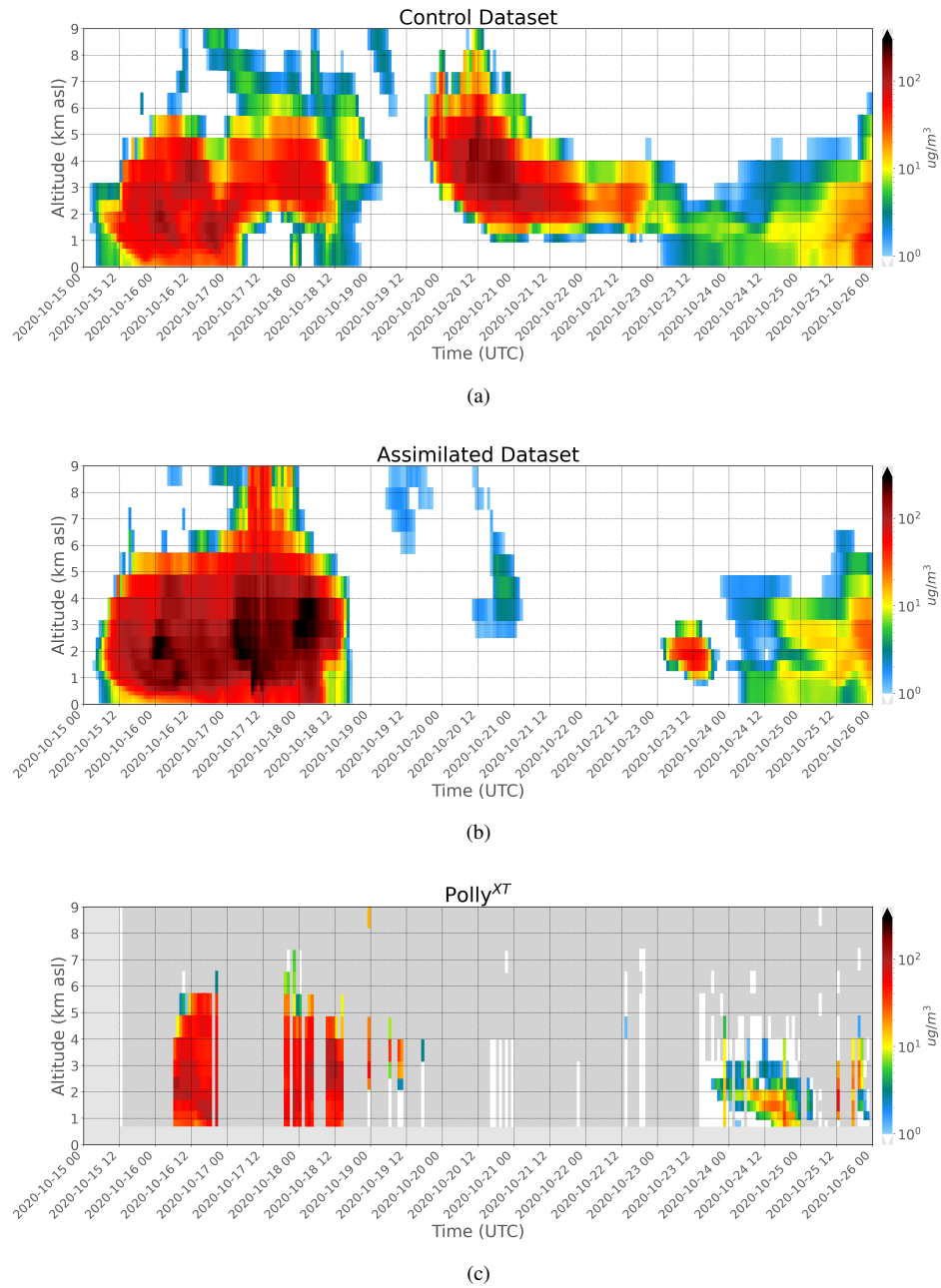


**Figure 7.** Collocated vertical dust concentrations for the control run (7a), assimilated run (7b) and Polly<sup>XT</sup> observations (7c) at the Antikythera, Greece, station for the 15-25<sup>th</sup> of October 2020.

### 3.3 Satellite-Based Evaluation

MIDAS and LIVAS satellite observations were sourced to complement ground-based observations from AERONET and Polly<sup>XT</sup>. MIDAS provides aerosol observations at wide spatial coverage with a fine spatial resolution, whereas LIVAS provides vertically resolved retrievals at fine vertical resolution.

400 A comparison of the model runs with observations from MIDAS is depicted in Figs. 8a and 8b, where the highlighted areas indicate locations of significant discrepancies between control and assimilated model runs. As expected, in both simulations, areas of high AOD are concentrated at the Sahel, a dust source region active throughout the year with dust activity peaking in spring (Ravi, 2011; Middleton, 2001). Introducing the Aeolus assimilated wind dataset improves cohesion between simulated and observed values. This is especially true over the Central Mediterranean, where positive bias is reduced by 45%, attributed  
405 to the control run simulating an anticyclone not seen in the assimilated run. Furthermore, a reduction in negative bias by 8% is achieved over the Fertile Crescent (Mesopotamia), a dust-source region that became active from 2006 onwards due to prolonged periods of drought (Kelley, 2015).

Dust events close to the domain boundaries are less resolved. In particular, discrepancies East of the Caspian Sea are noted. The relative error of simulating events increases with the magnitude of the event. Hence strong events close to the boundaries  
410 inherit a larger error relative to events in the inner domain, which is the case for this study period. Fig. 8c shows the observed AOD values averaged for the period 14-25<sup>th</sup> of October 2020 with three circled localities where the model, in both runs, underestimated AOD values. AOD present at location 1 is most likely derived from the Bodélé depression, an enclosed basin of alluvium silts deflated by a low-level jet transporting dust south to the gulf of Guinea (Todd, 2007; Engelstaedter, 2007; Washington, 2005). The Bodélé depression has been the subject of various past literature due to the inability of global dust  
415 models with a coarse horizontal resolution to accurately depict AOD in the area (Bou, 2009; Huneus, 2011; Haustein, 2012). Location 2 spans over the Mauritania-Mali source area, the Taoudenni basin, where the modelled, northerly winds displace aerosols further South for both runs overestimating AOD values relative to MIDAS. While locations 1 and 2 are dust-source regions strongly affecting areas in North Africa, the North Atlantic Ocean, and the Mediterranean, location 3 is a critical dust-source influx for the EMME region. The underestimation of model AOD values in Mesopotamia has been related to the regime  
420 shift in dust activity from 2006 onwards (Notaro, 2015). It is apparent that the recent changes in land characterisation are not reflected within the current model land configuration scheme. In future versions of the regional WRF-Chem model, the model-observation discrepancies could be further analysed, and appropriate re-configurations can be implemented to accurately depict land use (change).

Using the LIVAS dataset allowed for the evaluation of vertical dust concentration as depicted by Fig. 9. In all instances, the  
425 dust resides up to 5-6 km with concentrations lower than 15  $\mu\text{g}/\text{m}^3$  at higher altitudes. This is consistent with past literature, which determined the upper altitudes of dust in the Mediterranean to fall within the range of 5-9 km (Alpert, 2004; Papayannis, 2005). However, simulated dust concentrations atop the Antikythera lidar reached a maxima of 10 km (Fig. 7c). Revealed by Fig. 9a, just off the Libyan coast, the control run simulated a dust plume related to the pronounced anticyclonic activity, which is neither present in the assimilated run nor the observed dust vertical profile. Both model runs overestimated dust concentrations

430 relative to LIVAS southwest from the Bodélé depression. The control run overestimated by approximately  $500 \mu\text{g}/\text{m}^3$  and the assimilated run by  $200 \mu\text{g}/\text{m}^3$ , which could be attributed to the discussion regarding location 1 (Fig 8c). For the 21<sup>st</sup> of October (Fig. 9b), a dust plume is observed at the coast of Egypt, also modelled by the assimilated run, but shifted by 1 degree South whilst is absent in the control run.

## Model evaluation through MIDAS AOD, 14-25<sup>th</sup> of October 2020

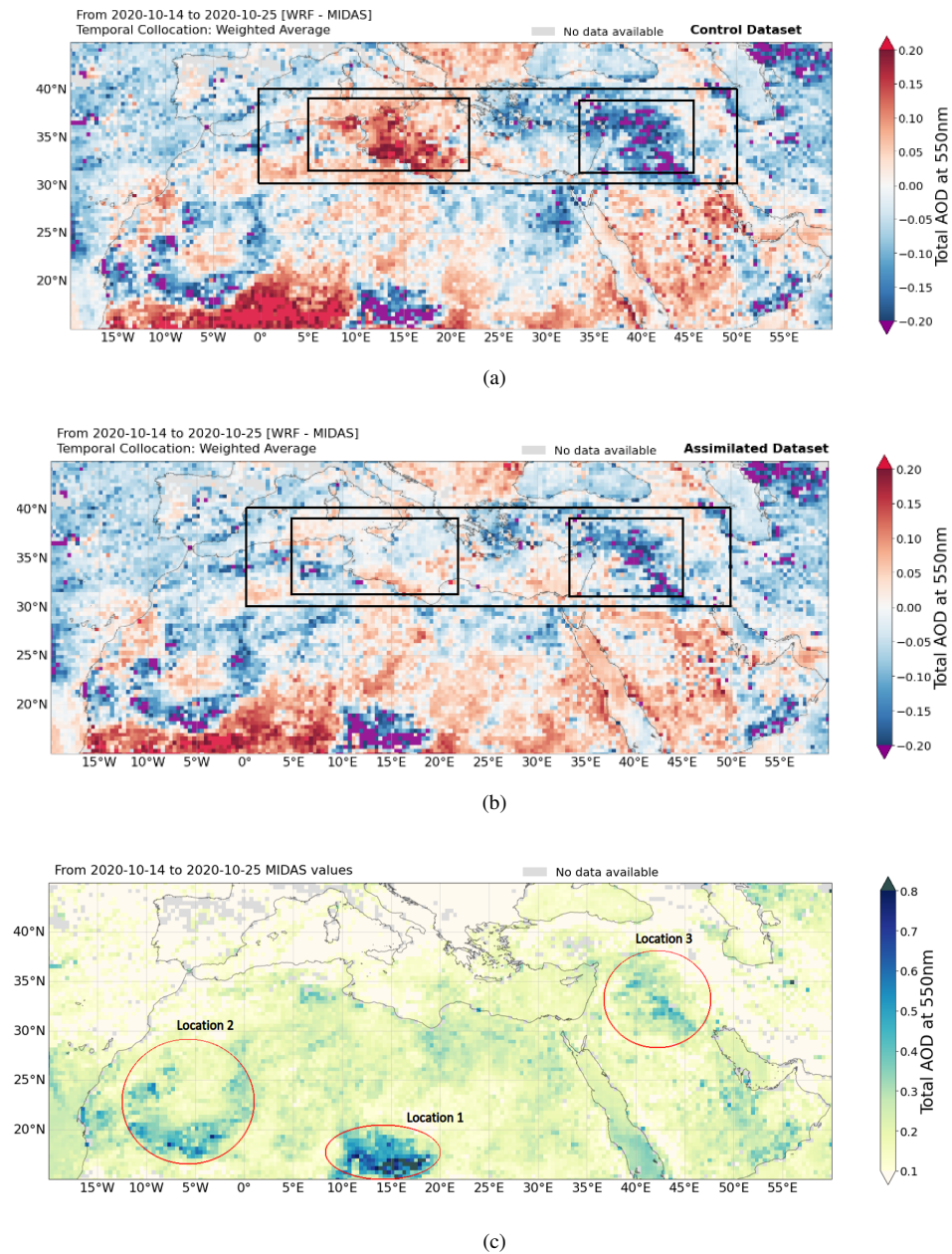


**Figure 8.** Time averaged differences in AOD (WRF-MIDAS) for the control run (8a) and the assimilated run (8b), where the black rectangles indicate regions of significant improvement when simulating conditions using the assimilated run. Additionally, 8c represents the observed MIDAS AOD values for the time-averaged period of 14-25<sup>th</sup> of October, where the highlighted red circles indicate locations where both runs underestimate AOD.

Only night-time profiles with a backscatter coefficient of more than  $0.0008 \text{ km}^{-1}\text{sr}^{-1}$  and a height greater than 180 m above  
435 surface elevation were used to ensure a reliable statistical comparison of model outputs with LIVAS products (Proestakis,  
2018). Additionally, observations were filtered within the limits of a dust optical depth  $\geq 0.01$  and  $> 4$  cloud-free profiles  
falling within the one-degree grid cell. Introducing these filters saw both model runs recording an increase in correlation  
coefficient and index of agreement and a reduction in normalised mean bias (NMB) and root mean square error (RMSE).  
However, this resulted in a drop in the number of sample counts from 3,874 to 2,037, limiting the availability of comparable  
440 observations. Thus, a comparison was made for the whole domain and the area spanning from  $0^\circ \text{ E}$ ,  $30^\circ \text{ N}$  to  $50^\circ \text{ E}$ ,  $40^\circ \text{ N}$   
rather than sub-regions, as conducted for MIDAS, and is summarised in Table 3.

It is apparent from both observation datasets that the introduction of the assimilated Aeolus wind fields improves the model  
predictive ability by reducing positive biases and improving the correlation of modelled products to observations. Comparison  
with MIDAS observations saw a substantial reduction in positive bias by 44% in the Central Mediterranean region, accom-  
445 panied by an increase in  $r$  by 0.19. This has been attributed to the control run simulating an anticyclone not present in the  
assimilated run. Over Mesopotamia, a reduction of negative bias of 17% is attained. To compensate for the small sample num-  
ber in the regions mentioned above, a statistical analysis has been performed for a box spanning from  $0^\circ \text{ E}$ ,  $30^\circ \text{ N}$  to  $50^\circ \text{ E}$ ,  $40^\circ$   
 $\text{N}$ , covering both the Central Mediterranean and Mesopotamia, which led to an increase in the sample pool. Within this area,  
significant improvements were recorded with an increase of  $r$  by 0.31, IOA by 0.18 and a reduction of positive bias by 23%.  
450 As observed in the statistical comparison with AERONET (section 3.2), comparing MIDAS observations to the whole domain  
reduces the improvements achieved using the assimilated dataset. This does not stand true for LIVAS, where data points are  
solely available atop CALIPSO-satellite tracks, and a synoptic comparison of all available overpasses improved  $r$  by 0.06,  
while reduced positive bias by 26% when using the assimilated products. Limiting the comparison within the  $0^\circ \text{ E}$ ,  $30^\circ \text{ N}$  to  
 $50^\circ \text{ E}$ ,  $40^\circ \text{ N}$  box reduced positive bias by 4% and RMSE by 0.19.



## Model evaluation through LIVAS vertical dust concentration for the 20<sup>th</sup> and 21<sup>st</sup> of October 2020

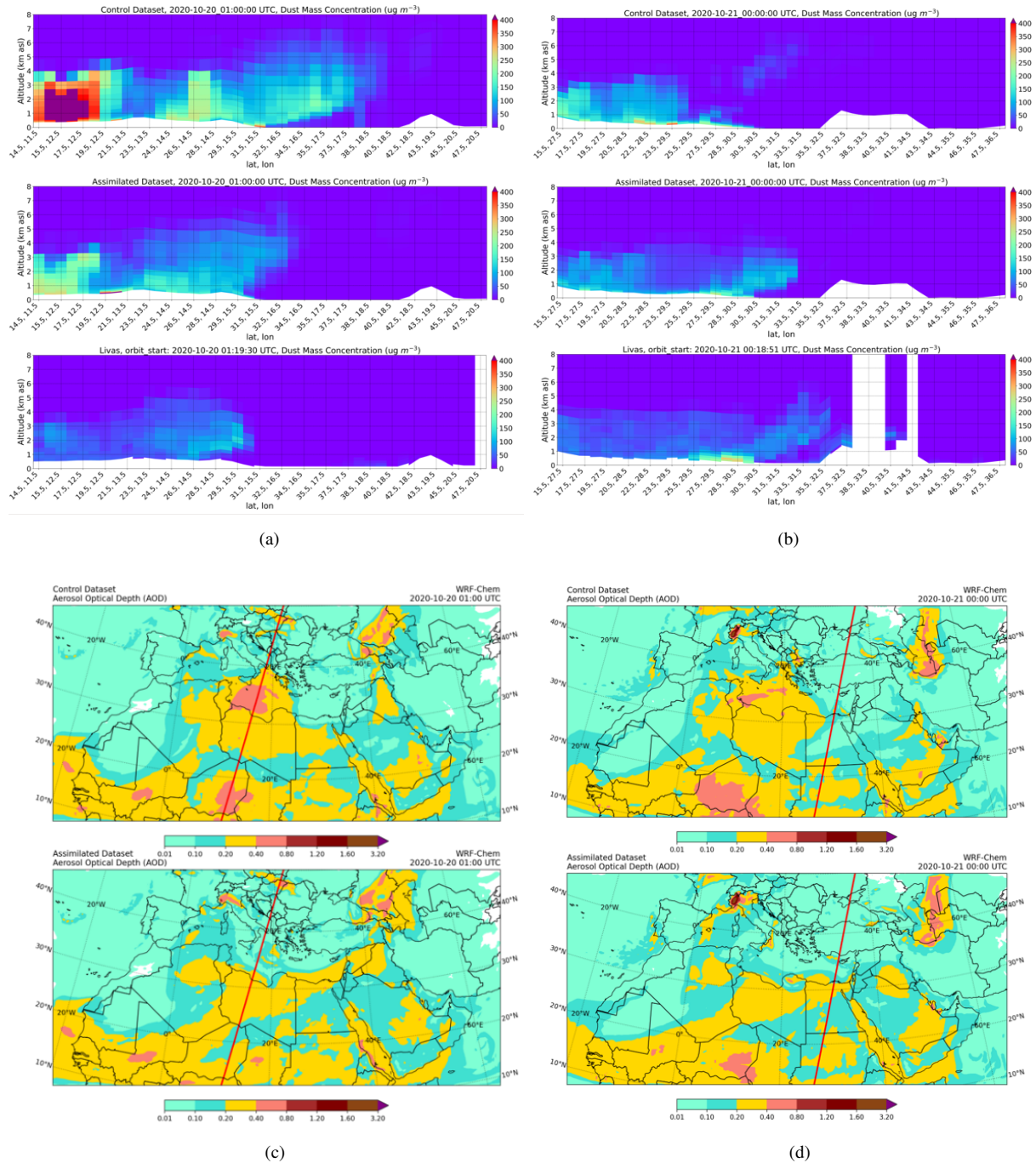


**Figure 9.** Collocated control and assimilated model runs to LIVAS depicting vertical dust concentrations for the dates; 2020-10-20-01:00 (9a) and 2020-10-21-00:00 (9b), along the CALIPSO tracks represented by the red lines in the horizontal AOD simulated values (9c, 9d), where for 9a and 9b the top panel represents the control run, the middle panel the assimilated run and the bottom panel LIVAS observations.

**Table 3.** Statistical comparison of modelled to observed products for MIDAS and LIVAS for the period 14-25<sup>th</sup> of October 2020.

Region	Whole Domain		0° E, 30° N to 50° E, 40° N		Mesopotamia		Central Mediterranean	
<b>Comparison with MIDAS</b>								
Datasets	Control	Assimilated	Control	Assimilated	Control	Assimilated	Control	Assimilated
Counts	18532 (100%)		3443 (18.6%)		915 (4.9%)		1345 (7.3%)	
r	0.52	0.54	0.32	0.63	0.49	0.60	0.53	0.72
IOA	0.71	0.72	0.53	0.71	0.52	0.64	0.70	0.81
NMB	57%	52%	52%	29%	-41%	-34%	68%	24%
<b>Comparison with LIVAS</b>								
Datasets	Control	Assimilated	Control	Assimilated				
Counts	2037 (100%)		325 (16%)					
r	0.36	0.40	-0.12	0.16	—		—	
RMSE	90	68	82	63				
NMB	48%	22%	26%	22%				

#### 455 4 Conclusions

The launch of the ESA's Aeolus satellite, acquiring wind profiles up to the lower stratosphere for the first time, was a significant step forward for Earth Observations. Aeolus filled a critical gap in the Global Observing System by providing vertically resolved winds over remote oceanic and vast continental areas not well covered by conventional wind observations. Aligned with the main scientific objective of the satellite mission, ECMWF, was the first meteorological centre that started the operational assimilation of Aeolus winds (January 2020), followed by other European institutes. Thanks to these activities, the beneficial impact of Aeolus winds on numerical weather prediction has been demonstrated via their implementation into global atmospheric models. This advancement in the forecast models' predictive skills is anticipated to materialise also in aerosol and air-quality simulations, acknowledging the determinant role of meteorology on the processes governing the life cycle components of airborne particles.

465 In the presented paper, the effect on aeolian dust prediction from the inclusion of the ECMWF-IFS Aeolus assimilated Rayleigh-clear and Mie-cloudy wind products within the WRF-Chem model in spring and autumn 2020 was studied. Focus was given to the broader Eastern Mediterranean and Middle East region, frequently affected by massive loads of mineral particles. The impact of the Aeolus dataset was more evident during the transitional October period compared to the spring months, where the maximum difference in dust concentration over the study region was  $20 \mu\text{g}/\text{m}^3$  at the atmospheric layer of 850 mb. 470 In October, distinct differences in dust concentrations were visualised, with values peaking over the Central Mediterranean in the control run and over the Levantine basin in the assimilated run. This suggested that the impact of the use of the assimilated dataset has temporal variation over the EMME region. Through further research, the observation regarding the improved

model predictability visualised only for the autumn months could be investigated to explain the driving forces responsible for the improvement.

475 The period of 14 to 25 October 2020 has been investigated for the Eastern Mediterranean and Middle East region, where anticyclonic conditions prevail in the Central and East Mediterranean region leading to the transport of aeolian dust particles. The dust numerical model outputs were evaluated against ground-based and satellite observations to ensure a complete and comprehensive assessment. Analysis of the October period revealed that in the control run, an anticyclone materialised over the domain, which was much less pronounced in the assimilated run. Comparison of the model results to both ground- and  
480 satellite-based observations, including; EMEP, AERONET, PollyXT, MIDAS and LIVAS, allowed for a thorough investigation of numerical dust outputs both horizontally and vertically. In all cases, using the Aeolus assimilated wind products improved the model predictive ability with increases in correlation coefficient and index of agreement and decreases in positive and negative biases. The most significant improvements were observed when the statistical analyses were performed over the EMME region, while comparisons with the whole simulated domain decreased the improvements. Specifically, for the period where a second  
485 anticyclone forms in the control run, the use of Aeolus resulted in a reduction of positive bias atop the anticyclone by 44% and an improvement in the correlation coefficient by 0.19. Through FLEXPART backwards-trajectory analysis, the source regions of aerosols were analysed. It was revealed that the control run had an influx of aerosols from continental Europe, while the assimilated run from the Saharan region. The benefits attained from the incorporation of the IFS assimilated Aeolus data solely regard the period of 14 to 25 October 2020, where anticyclonic conditions prevail in the EMME and Central Mediterranean  
490 regions. Even though the period of improvement is statistically negligible compared to longer timescales, the strong reductions in positive bias and underestimates highlight the importance of Aeolus in further dust research.

The case study can serve as a benchmark for future relevant studies with emphasis on long-term periods and other natural aerosol species, such as volcanic ash (Kampouri, 2022) and sea salt. Relying on the same concept, a similar study (Gkikas, 2022) for the western Sahara, hosting some of the most active dust sources of the planet (Ginoux, 2012), and the Tropical  
495 Atlantic Ocean, receiving large amounts of mineral particles exported from the Sahara Desert throughout the year, is in preparation. According to preliminary results in the framework of the JATAC campaign (Cape Verde, September 2021), there are evident modifications of the meteorological patterns. These are observed throughout the atmosphere, subsequently affecting the evolution of the Saharan dust plumes, which are more realistically represented in the numerical experiments initialised after incorporating IFS assimilated Aeolus wind fields. An interesting aspect for future works would be a holistic approach for  
500 the assimilation experiments relying solely on Aeolus retrievals. More specifically, an investigation into the feasibility of the implementation of Aeolus wind profiles in regional atmospheric-dust models for producing meteorological and dust analyses could be carried out. These can be utilised to initialise short- to medium-term forecasts. Finally, a better representation of the simulated aerosol fields from Aeolus wind implementation will result in an improved assessment of the aerosol-induced perturbations of the Earth-Atmosphere radiation budget with accompanying positive impacts on numerical weather prediction  
505 (Pérez, 2006; Gkikas, 2018; Benedetti, 2018). Thus, fulfilling the main scientific objective of the Aeolus satellite mission.

## Appendix A

### A1

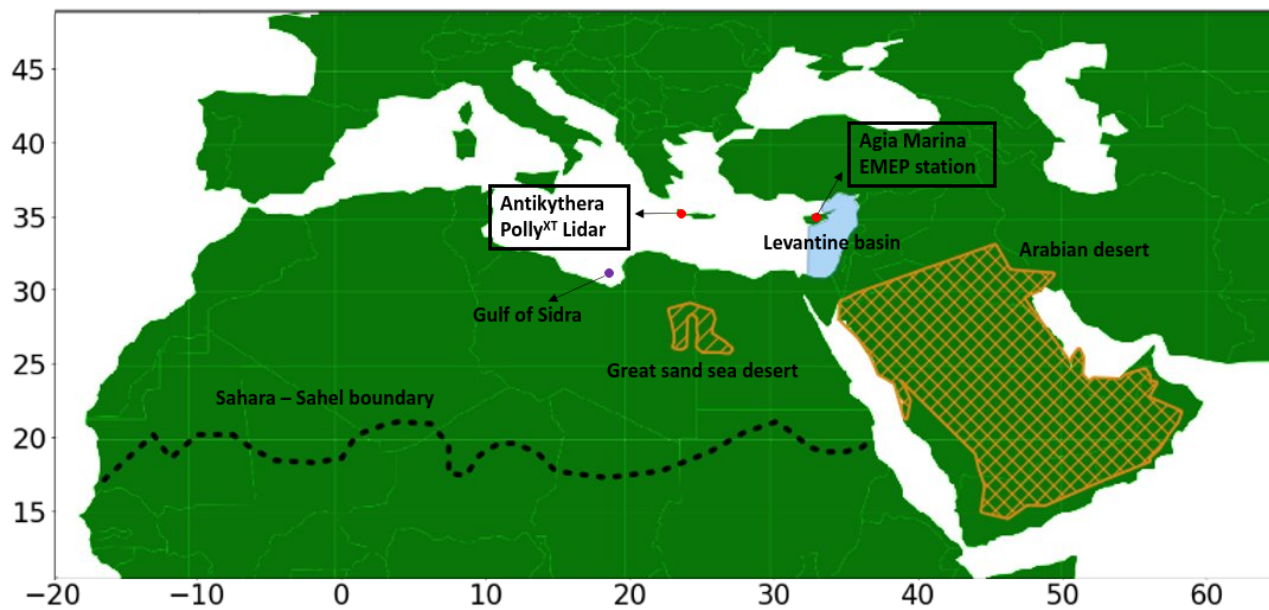


**Figure A1.** Model domain used in the WRF-Chem simulations alongside some locations and observation stations mentioned in the text.

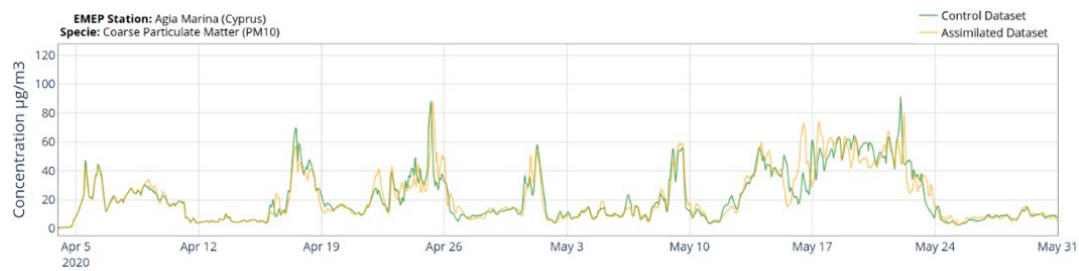
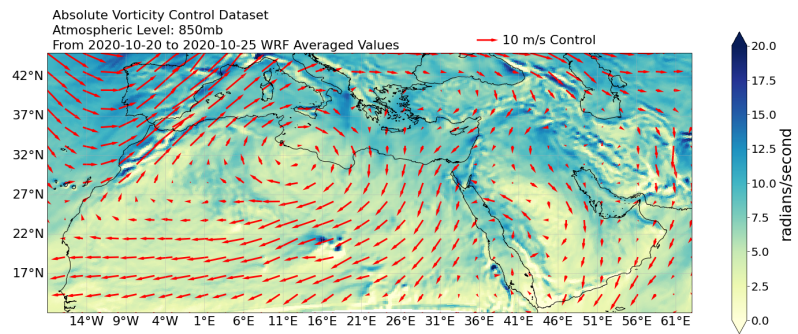
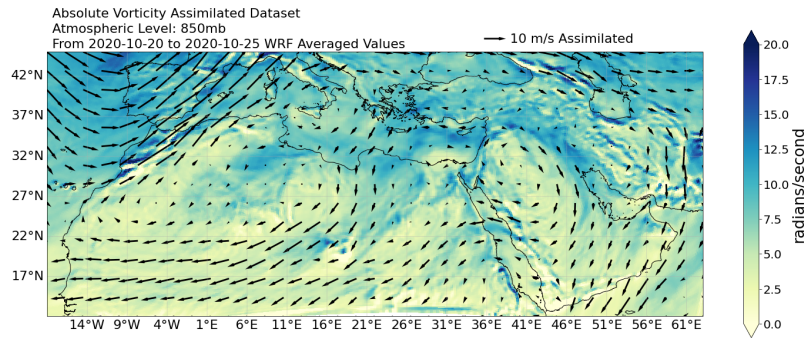


**Figure A2.** Comparison of PM10 at the EMEP Station at Ayia Marina, Cyprus, between the WRF-Chem simulations in spring, where the green line represents the control run and the yellow the assimilated run.



(a)



(b)

**Figure A3.** Comparison of model vorticity for control (A3a) and assimilated (A3b) runs (20-25 October 2020), where the wind vectors are represented in red for the control run and black for the assimilated run.

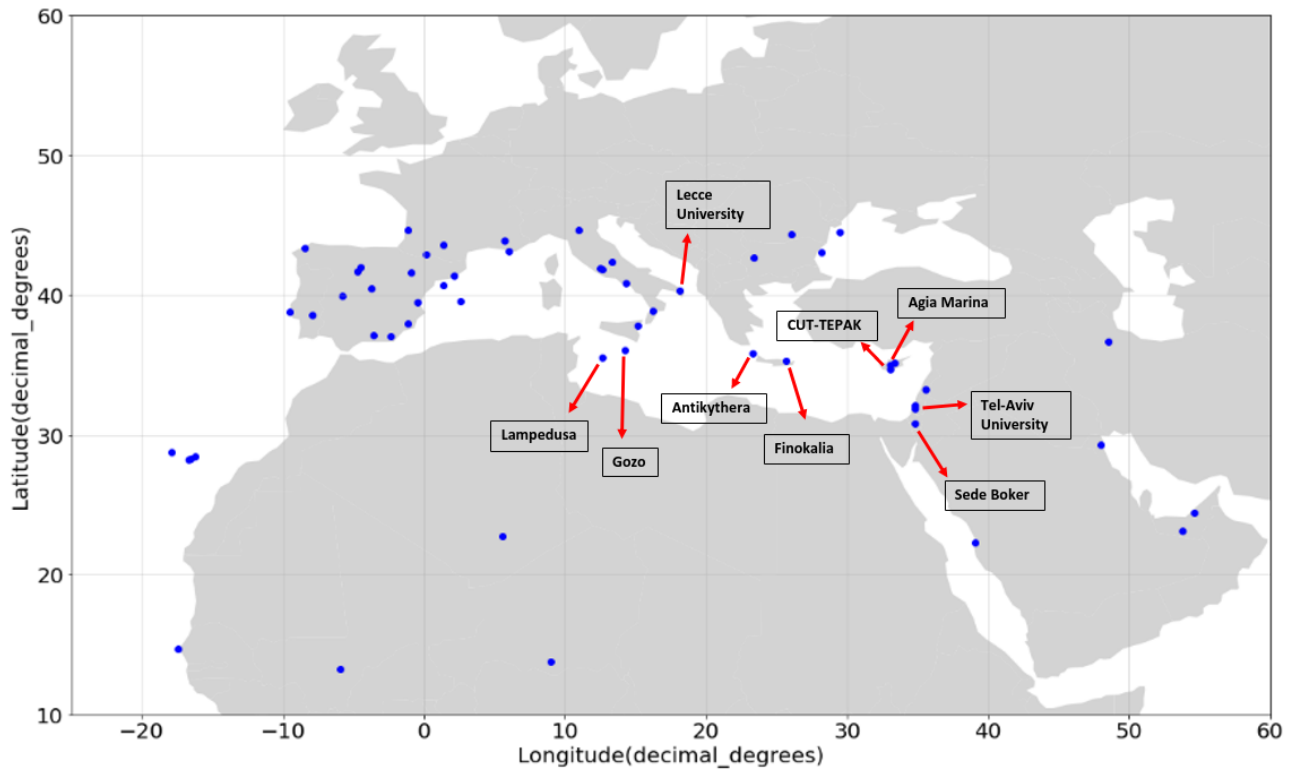


**Figure A4.** Map of all the AERONET stations within the constructed domain with available observations for the period of 18/09/2020 to 01/11/2020, used for the model evaluation. Additionally, the stations used in the main text are highlighted.

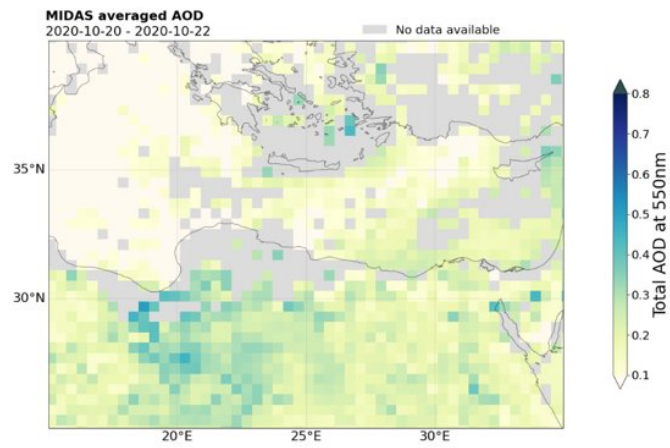


**Figure A5.** MIDAS AOD values for the time averaged period of 20-22<sup>nd</sup> of October 2020 for the model domain area surrounding the Polly<sup>XT</sup> lidar instrument.



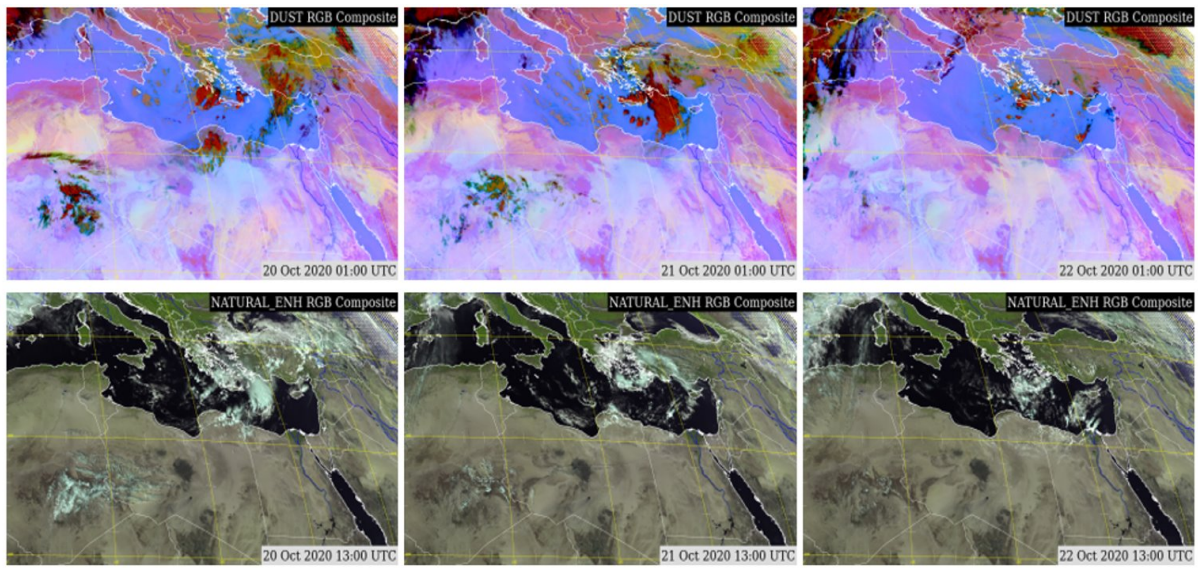


**Figure A6.** Representation of satellite imagery over Antikythera from the 20th to the 22nd of October, where in the top panel the Dust RGB composite colour is shown for night-time imagery at 01:00 UTC and in the bottom panel the natural enhanced imagery is shown for 13:00 UTC. The images of Fig. A6 are property of ©EUMETSAT [2020].

**Table A1.** WRF-Chem model configuration options used in the simulations.

<b>Process</b>	<b>Option</b>	<b>Reference</b>
<i>Microphysics</i>	Morrison 2-moment scheme	Morrison (2005)
<i>Land-Surface</i>	NOAH Land Surface Model	Chen (2001)
<i>Boundary Layer</i>	Yonesi University (YSU) Planetary Boundary Layer	Hong (2006)
<i>Cumulus</i>	Grell 3D Ensemble Scheme	Grell (2002)
<i>Surface Layer</i>	MM5 Similarity Surface Layer Scheme	Zhang (1982)
<i>Radiation</i>	Rapid Radiative Transfer Model (RRTMG)	Iacono (2008)
<i>Gas Phase Chemistry</i>	Regional Atmospheric Chemistry Mechanism (RACM)	Stockwell (1997)
<i>Aerosols</i>	Model Aerosol Dynamics Model for Europe (MADE) Secondary Organic Aerosol Model (SORGAM)	Ackerman (1998) Schell (2001)

*Author contributions.* Kiriakidis Pantelis: Produced the model experiments, Data Collection, Data Analysis and Writing of the Manuscript. Gkikas Antonis: Produced the model experiments, Data Collection, Contributed to the scientific discussion and Reviewed the Manuscript. 510 Papangelis Georgios: Produced the model experiments, Data Collection and Contributed to the scientific discussion. Christoudias Theodoros: Contributed to the scientific discussion and Reviewed the Manuscript. Kushta Jonilda: Contributed to the scientific discussion. Proestakis Emmanouil: Data Collection and Contributed to the scientific discussion. Kampouri Anna: Data Collection and Contributed to the scientific discussion. Marinou Eleni: Data Collection and Contributed to the scientific discussion. Drakaki Eleni: Contributed to the scientific discussion. Benedetti Angela: Contributed to the scientific discussion. Rennie Michael: Contributed to the scientific discussion. Retscher Christian: 515 Contributed to the scientific discussion. Straume Anne Grete: Contributed to the scientific discussion. Dandocsi Alexandru: Contributed to the scientific discussion. Amiridis Vasilis: Contributed to the scientific discussion. Sciare Jean: Contributed to the scientific discussion.

*Competing interests.* The authors declare that they have no conflict of interest.

*Acknowledgements.* Gkikas A. acknowledges support by the Hellenic Foundation for Research and Innovation (H.F.R.I.) under the “2nd Call for H. F. R. I. Research Projects to support Post-Doctoral Researchers” (project acronym: ATLANTAS, project number: 544). The 520 NEWTON project has been supported by ESA under Contract No. 4000133130/20/I-BG// Aeolus+ Innovation (Aeolus+I). The Cyprus Institute acknowledges support from the EMME-CARE project funded from the European Union’s Horizon 2020 Research and Innovation Programme (under grant agreement no. 856612) and the Cyprus Government, and ACCEPT which is co-financed by the Norwegian Financial Mechanism (85 %) and the Republic of Cyprus (15 %) in the framework of the programming period 2014–2021. We thank EARLINET (<https://www.earlinet.org/>, last access: 1 Feb. 2023), ACTRIS (<https://www.actris.eu>, last access: 1 Feb. 2023), PollyNET 525 (<https://polly.tropos.de/>, last access: 1 Feb. 2023), AERONET (<https://aeronet.gsfc.nasa.gov/>, last access: 1 Feb. 2023) and AERONET-Europe for the data collection, calibration, processing and dissemination. We thank NASA/LaRC/ASDC for making available the CALIPSO products which are used to build LIVAS products.

## References

- Ackerman, S., Strabala, K., Menzel, W., Frey, R., Moeller, C., Gumley, L. & S. Discriminating clear sky from clouds with MODIS". *Journal Of Geophysical Research: Atmospheres*. **103**, 32141-32157 (1998)
- 530 Alonso-Pérez, S., Cuevas, E., Querol, X., Guerra, J. & Pérez, C. African dust source regions for observed dust outbreaks over the Subtropical Eastern North Atlantic region, above 25 N. *Journal Of Arid Environments*. **78** pp. 100-109 (2012)
- Ahmadov, R., McKeen, S., Robinson, A., Bahreini, R., Middlebrook, A., Gouw, J., Meagher, J., Hsie, E., Edgerton, E., Shaw, S., Trainer, M. & R. A volatility basis set model for summertime secondary organic aerosols over the eastern United States in 2006". *Journal Of*
- 535 *Geophysical Research: Atmospheres*. **117**, - (2012)
- Alpert, P., Kishcha, P., Shtivelman, A., Krichak, S. & Joseph, J. Vertical distribution of Saharan dust based on 2.5-year model predictions. *Atmospheric Research*. **70**, 109-130 (2004)
- Amiridis, V., Wandinger, U., Marinou, E., Giannakaki, E., Tsekeri, A., Basart, S., Kazadzis, S., Gkikas, A., Taylor, M., Baldasano, J. & Ansmann, A. Optimizing CALIPSO Saharan dust retrievals, *Atmos. Chem. Phys.* **13**, 12089-12106, (2013)
- 540 Angström, A. On the Atmospheric Transmission of Sun Radiation and on Dust in the Air. *Geografiska Annaler*. **11**, 156-166, (1929)
- Ansmann, A., Mamouri, R., Hofer, J., Baars, H., Althausen, D. & Abdullaev, S. Dust mass, cloud condensation nuclei, and ice-nucleating particle profiling with polarization lidar: updated POLIPHON conversion factors from global AERONET analysis, *Atmos. Meas. Tech.* **12** pp. 4849-4865, (2019), <https://doi.org/10.5194/amt-12-4849-2019>,
- Baars, H., Herzog, A., Heese, B., Ohneiser, K., Hanbuch, K., Hofer, J., Yin, Z., Engelmann, R. & Wandinger, U. Validation of Aeolus wind
- 545 products above the Atlantic Ocean. *Atmospheric Measurement Techniques*. **13**, 6007-6024 (2020)
- Barnard, J., Fast, J., Paredes-Miranda, G., Arnott, W. & Laskin, A. Evaluation of the WRF-Chem" Aerosol Chemical to Aerosol Optical Properties" Module using data from the MILAGRO campaign. *Atmospheric Chemistry And Physics*. **10**, 7325-7340 (2010)
- Basart, S., Pérez, C., Cuevas, E., Baldasano, J. & Gobbi, G. Aerosol characterization in Northern Africa, Northeastern Atlantic, Mediterranean basin and Middle East from direct-sun AERONET observations. *Atmospheric Chemistry And Physics*. **9**, 8265-8282 (2009)
- 550 Ben-Asher, M., Haviv, I., Roering, J. & Crouvi, O. The potential influence of dust flux and chemical weathering on hillslope morphology: Convex soil-mantled carbonate hillslopes in the Eastern Mediterranean. *Geomorphology*. **341** pp. 203-215 (2019)
- Benedetti, A. & Vitart, F. Can the direct effect of aerosols improve subseasonal predictability?. *Monthly Weather Review*. **146**, 3481-3498 (2018)
- Bou Karam, D., Flamant, C., Tulet, P., Chaboureaud, J., Dabas, A. & Todd, M. Estimate of Sahelian dust emissions in the intertropical
- 555 discontinuity region of the West African monsoon. *J. Geophys. Res.* **114**, D13106 (2009)
- Brioude, J., Arnold, D., Stohl, A., Cassiani, M., Morton, D., Seibert, P., Angevine, W., Evan, S., Dingwell, A., Fast, J. & Others The Lagrangian particle dispersion model FLEXPART-WRF version 3.1. *Geoscientific Model Development*. **6**, 1889-1904 (2013)
- Cavazos-Guerra, C. & Todd, M. Model simulations of complex dust emissions over the Sahara during the West African monsoon onset. *Advances In Meteorology*. **2012** (2012)
- 560 Chaibou, A., Ma, X., Kumar, K., Jia, H., Tang, Y. & Sha, T. Evaluation of dust extinction and vertical profiles simulated by WRF-Chem with CALIPSO and AERONET over North Africa. *Journal Of Atmospheric And Solar-Terrestrial Physics*. **199** pp. 105213 (2020)
- Chedin, A., Capelle, V. & Scott, N. Detection of IASI dust AOD trends over Sahara: How many years of data required?. *Atmospheric Research*. **212** pp. 120-129 (2018)

- Chen, F. & JDudhia Coupling an Advanced Land Surface-Hydrology Model with the Penn State-NCAR MM5 Modeling System. Part I: Model Implementation and Sensitivity. *Mon. Wea. Rev.* **129** pp. 569-585 (2001)
- 565 D'Amico, G., Amodeo, A., Baars, H., Biniotoglou, I., Freudenthaler, V., Mattis, I., Wandinger, U. & Pappalardo, G. EARLINET Single Calculus Chain—overview on methodology and strategy, *Atmos. Meas. Tech.* **8** pp. 4891-4916, (2015), <https://doi.org/10.5194/amt-8-4891-2015>,
- Darmenova, K., Sokolik, I., Shao, Y., Marticorena, B. & Bergametti, G. Development of a physically based dust emission module within the Weather Research and Forecasting (WRF) model: Assessment of dust emission parameterizations and input parameters for source regions in Central and East Asia. *Journal Of Geophysical Research: Atmospheres.* **114** (2009)
- 570 De-Châtel, F. The role of drought and climate change in the Syrian uprising: Untangling the triggers of the revolution. *Middle Eastern Studies.* **50**, 521-535 (2014)
- Deng, A., Stauffer, D., Dudhia, J., Otte, T. & Hunter, G. Update on analysis nudging FDDA in WRF-ARW. *Proceedings Of The 8th WRF Users' Workshop.* pp. 35 (2007)
- 575 Deng, A., Stauffer, D., Gaudet, B. & Hunter, G. A rapidly relocatable high-resolution WRF system for military-defense, aviation and wind energy. *13th Annual WRF Users' Workshop.* pp. 25-29 (2012)
- Dubovik, O. & King, M. A flexible inversion algorithm for retrieval of aerosol optical properties from Sun and sky radiance measurements. *Journal Of Geophysical Research: Atmospheres.* **105**, 20673-20696 (2000)
- 580 Dubovik, O., Sinyuk, A., Lapyonok, T., Holben, B., Mishchenko, M., Yang, P., Eck, T., Volten, H., Munoz, O., Veihelmann, B. & Zande, W. Application of spheroid models to account for aerosol particle nonsphericity in remote sensing of desert dust. *J. Geophys. Res.-Atmos.* **111**, D11208 (2006), <https://doi.org/10.1029/2005JD006619>,
- Eck, T., Holben, B., Reid, J., Dubovik, O., Smirnov, A., O'Neill, N., Slutsker, I. & Kinne, S. Wavelength dependence of the optical depth of biomass burning, urban, and desert dust aerosols. *J. Geophys. Res.* **104** pp. 31333-31349, (1999)
- 585 Engelstaedter, S., Tegen, I. & Washington, R. North African dust emissions and transport. *Earth-Science Reviews.* **79**, 73-100 (2006)
- Engelstaedter, S. & Washington, R. Atmospheric controls on the annual cycle of North African dust. *Journal Of Geophysical Research: Atmospheres.* **112** (2007)
- Flaounas, E., Kotroni, V., Lagouvardos, K., Klose, M., Flamant, C. & Giannaros, T. Sensitivity of the WRF-Chem (V3. 6.1) model to different dust emission parametrisation: assessment in the broader Mediterranean region. *Geoscientific Model Development.* **10**, 2925-2945 (2017)
- 590 Flocas, H., Maheras, P., Karacostas, T., Patrikas, I. & Anagnostopoulou, C. A 40-year climatological study of relative vorticity distribution over the Mediterranean. *Int. J. Climatol.* **21** pp. 1759-1778, (2001)
- Formenti, P., Andreae, M., Andreae, T., Galani, E., Vasaras, A., Zerefos, C., Amiridis, V., Orlovsky, L., Karnieli, A., Wendisch, M. & Others Aerosol optical properties and large-scale transport of air masses: Observations at a coastal and a semiarid site in the eastern Mediterranean during summer 1998. *Journal Of Geophysical Research: Atmospheres.* **106**, 9807-9826 (2001)
- 595 Fotiadi, A., Hatzianastassiou, N., Drakakis, E., Matsoukas, C., Pavlakis, K., Hatzidimitriou, D., Gerasopoulos, E., Mihalopoulos, N. & Vardavas, I. Aerosol physical and optical properties in the Eastern Mediterranean Basin, Crete, from Aerosol Robotic Network data. *Atmospheric Chemistry And Physics.* **6**, 5399-5413 (2006)
- Gelaro, R., McCarty, W., Suárez, M., Todling, R., Molod, A., Takacs, L., Randles, C., Darmenov, A., Bosilovich, M., Reichle, R., Wargan, K., Coy, L., Cullather, R., Draper, C., Akella, S., Buchard, V., Conaty, A., Silva, A., Gu, W., Kim, G., Koster, R., Lucchesi, R., Merkova, D., Nielsen, J., Partyka, G., Pawson, S., Putman, W., Rienecker, M., Schubert, S., Sienkiewicz, M. & Zhao, B. The Modern-Era Retrospective Analysis for. *Research And Applications.* **Version 2** pp. -2 , (2017), <https://doi.org/10.1175/JCLI-D-16-0758.1>,
- 600

- Georgiou, G., Christoudias, T., Proestos, Y., Kushta, J., Hadjinicolaou, P. & Lelieveld, J. Air quality modelling in the summer over the eastern Mediterranean using WRF-Chem: chemistry and aerosol mechanism intercomparison, *Atmos. Chem. Phys.* **18** pp. 1555-1571, (2018), <https://doi.org/10.5194/acp-18-1555-2018>,
- 605 Giles, D., Sinyuk, A., Sorokin, M., Schafer, J., Smirnov, A., Slutsker, I., Eck, T., Holben, B., Lewis, J., Campbell, J. & Others Advancements in the Aerosol Robotic Network (AERONET) Version 3 database—automated near-real-time quality control algorithm with improved cloud screening for Sun photometer aerosol optical depth (AOD) measurements. *Atmospheric Measurement Techniques*. **12**, 169-209 (2019)
- Gillette, D. & Hanson, K. Spatial and temporal variability of dust production caused by wind erosion in the United States. *Journal Of Geophysical Research: Atmospheres*. **94**, 2197-2206 (1989)
- 610 Ginoux, P., Chin, M., Tegen, I., Prospero, J., Holben, B., Dubovik, O. & Lin, S. Sources and distributions of dust aerosols simulated with the GOCART model. *J. Geophys. Res.* **106**, 20255- 20273, (2001)
- Ginoux, P., Prospero, J., Gill, T., Hsu, N. & Zhao, M. Global-scale attribution of anthropogenic and natural dust sources and their emission rates based on MODIS Deep Blue aerosol products. *Reviews Of Geophysics*. **50** (2012)
- Grell, G. A generalized approach to parameterizing convection combining ensemble and data assimilation techniques. *Geophysical Research Letters*. **29** pp. 10-13, (2002)
- 615 Grell, G., Peckham, S., Schmitz, R., McKeen, S., Frost, G., Skamarock, W. & Eder, B. Fully coupled “online” chemistry within the WRF model. *Atmospheric Environment*. **39**, 6957-6975 (2005)
- Guenther, A., Jiang, X., Heald, C., Sakulyanontvittaya, T., Duhl, T., Emmons, L. & Wang, X. The model of emissions of gases and aerosols from nature version 2.1 (MEGAN2.1): An extended and updated framework for modeling biogenic emissions. *Geoscientific Model Development*. **5** pp. 1471-1492, (2012),
- 620 Gkikas, A., Hatzianastassiou, N., Mihalopoulos, N., Katsoulis, V., Kazadzis, S., Pey, J., Querol, X. & Torres, O. The regime of intense desert dust episodes in the Mediterranean based on contemporary satellite observations and ground measurements. *Atmospheric Chemistry And Physics*. **13**, 12135-12154 (2013)
- Gkikas, A., Basart, S., Hatzianastassiou, N., Marinou, E., Amiridis, V., Kazadzis, S., Pey, J., Querol, X., Jorba, O., Gassó, S. & Others Mediterranean intense desert dust outbreaks and their vertical structure based on remote sensing data. *Atmospheric Chemistry And Physics*. **16**, 8609-8642 (2016)
- 625 Gkikas, A., Obiso, V., Perez Garcia-Pando, C., Jorba, O., Hatzianastassiou, N., Vendrell, L., Basart, S., Solomos, S., Gassó, S. & Baldasano, J. Direct radiative effects during intense Mediterranean desert dust outbreaks. *Atmospheric Chemistry And Physics*. **18**, 8757-8787 (2018)
- Gkikas, A., Proestakis, E., Amiridis, V., Kazadzis, S., Di Tomaso, E., Tsekeri, A., Marinou, E., Hatzianastassiou, N. & Pérez Garcí’a-Pando, C. ModIs Dust AeroSol (MIDAS): a global fine-resolution dust optical depth data set. *Atmospheric Measurement Techniques*. **14**, 309-334 (2021),
- 630 Gkikas, A., Proestakis, E., Amiridis, V., Kazadzis, S., Di Tomaso, E., Marinou, E., Hatzianastassiou, N., Kok, J. & Garcí’a-Pando, C. Quantification of the dust optical depth across spatiotemporal scales with the MIDAS global dataset (2003–2017). *Atmospheric Chemistry And Physics*. **22**, 3553-3578 (2022)
- 635 Gkikas, A., Papangelis, G., Drakaki, E., Proestakis, E., Kampouri, A., Marinou, E., Tschla, M., Spyrou, C., Benedetti, A., Rennie, M., Paschou, P., Siomos, N., Baars, H., Straume, A.G., Retscher, C., Dandocsi, A., Engelmann, R., Skupin, A., Althausen, D., Wandinger, U., Yin, Z., Zenk, C. & Amiridis, V. Assessing the impact of Aeolus wind data assimilation on the numerical simulations of Saharan dust outflows towards the Tropical Atlantic Ocean. *Aeolus 3rd Anniversary Conference, 28/3 – 1/4/2022, Taormina, Italy.* (2022)

- Hachicha, A., Al-Sawafta, I. & Said, Z. Impact of dust on the performance of solar photovoltaic (PV) systems under United Arab Emirates weather conditions. *Renewable Energy*. **141** pp. 287-297 (2019)
- 640 Haseler, J. Early-delivery suite. (European Centre for Medium-Range Weather Forecasts,2004)
- Hatzaki, M., Flocas, H., Simmonds, I., Kouroutzoglou, J., Keay, K. & Rudeva, I. Seasonal aspects of an objective climatology of anticyclones affecting the Mediterranean. *Journal Of Climate*. **27**, 9272-9289 (2014),
- Haustein, K. Atmospheric dust modeling from meso to global scales with the online NMMB/BSC-Dust model—Part 2: Experimental cam-  
645 paigns in northern Africa, *Atmos. Chem. Phys.* **12** pp. 2933-2958, (2012),
- Heinold, B., Knippertz, P., Marsham, J., Fiedler, S., Dixon, N., Schepanski, K., Laurent, B. & Tegen, I. The role of deep convection and nocturnal low-level jets for dust emission in summertime West Africa: Estimates from convection-permitting simulations. *Journal Of Geophysical Research: Atmospheres*. **118**, 4385-4400 (2013)
- Holben, B., Eck, T., Slutsker, I., Tanre, D., Buis, J., Setzer, A., Vermote, E., Reagan, J., Kaufman, Y., Nakajima, T., Lavenue, F., Jankowiak, I. & Smirnov, A. AERONET – A federated instrument network and data archive for aerosol characterization, *Remote Sens. Environ.* **66**  
650 pp. 1-16, (1998), [https://doi.org/10.1016/S0034-4257\(98\)00031-5](https://doi.org/10.1016/S0034-4257(98)00031-5),
- Hong, S., Noh, Y. & Dudhia, J. A new vertical diffusion package with an explicit treatment of entrainment processes. *Monthly Weather Review*. **134** pp. 2318-2341, (2006), <http://journals.ametsoc.org/doi/abs/10.1175/MWR3199.1>,
- Hubanks, P., Platnick, S., King, M. & Ridgway, R. MODIS Atmosphere L3 Gridded Product Algorithm Theoretical Basis Document (ATBD) & Users Guide, ATBD Reference Number: L3 ATBD C6 2018 04 11. (2018),  
655
- Huneus, N. Global dust model intercomparison in AeroCom phase I, *Atmos. Chem. Phys.* **11** pp. 7781-7816, (2011)
- Iacono, M., Delamere, J., Mlawer, E., Shephard, M., Clough, S., Collins, W. & M. Radiative forcing by long-lived greenhouse gases: Calculations with the AER radiative transfer models". *Journal Of Geophysical Research*. **113** (2008)
- Ioannidou, L. & Yau, M. A climatology of the Northern Hemisphere winter anticyclones. *J. Geophys. Res.* **113**, D08119 (2008),
- 660 Isaksen, L. & Rennie, M. A preliminary evaluation of using Aeolus L2B Winds in ECMWF's NWP system, with focus on the tropical region. *Living Planet Symposium, Milan, Italy*. pp. 13-17 (2019)
- Janssens-Maenhout, G., Dentener, F., Van Aardenne, J., Monni, S., Pagliari, V., Orlando, L., Klimont, Z., Kurokawa, J., Akimoto, H., Ohara, T., Wankmueller, R., Battye, B., Grano, D., Zuber, A. & Keating, T. EDGAR-HTAP: a Harmonized Gridded Air Pollution Emission Dataset Based on National Inventories. *EUR 25229 EN*. (2012), JRC68434
- 665 Kalivitis, N., Gerasopoulos, E., Vrekoussis, M., Kouvarakis, G., Kubilay, N., Hatzianastassiou, N., Vardavas, I. & Mihalopoulos, N. Dust transport over the eastern Mediterranean derived from Total Ozone Mapping Spectrometer, Aerosol Robotic Network, and surface measurements. *Journal Of Geophysical Research: Atmospheres*. **112** (2007)
- Kampouri, A., Amiridis, V., Solomos, S., Gialitaki, A., Marinou, E., Spyrou, C., Georgoulas, A., Akritidis, D., Papagiannopoulos, N., Mona, L., Scollo, S., Tsihla, M., Tsikoudi, I., Pytharoulis, I., Karacostas, T. & Zanis, P. Investigation of Volcanic Emissions in the Mediterranean: "The Etna-Antikythera Connection". *Atmosphere*. **12**, 40 (2021), <https://doi.org/10.3390/atmos12010040>,  
670
- Kampouri, A., Amiridis, V., Gkikas, A., Gialitaki, A., Marinou, E., Proestakis, E., Benedetti, A., Rennie, M., Misios, S., Papangelis, G., Mona, L., Scollo, S., Vasardani, O., Zanis, P. & Straume, A.G. First numerical experiments assessing the impact of Aeolus wind data assimilation on volcanic ash dispersion. *Aeolus 3rd Anniversary Conference, 28/3 – 1/4/2022, Taormina, Italy*. (2022)
- Kanatani, K., Ito, I., Al-Delaimy, W., Adachi, Y., Mathews, W. & Ramsdell, J. Desert dust exposure is associated with increased risk of  
675 asthma hospitalization in children. *American Journal Of Respiratory And Critical Care Medicine*. **182**, 1475-1481 (2010)

- Kang, J., Yoon, S., Shao, Y. & Kim, S. Comparison of vertical dust flux by implementing three dust emission schemes in WRF/Chem. *Journal Of Geophysical Research: Atmospheres*. **116** (2011)
- Kelley, C., Mohtadi, S., Cane, M., Seager, R. & Kushnir, Y. Climate change in the Fertile Crescent and implications of the recent Syrian drought. *Proceedings Of The National Academy Of Sciences*. **112**, 3241-3246 (2015)
- 680 Klingmüller, K., Pozzer, A., Metzger, S., Stenchikov, G. & Lelieveld, J. Aerosol optical depth trend over the Middle East. *Atmospheric Chemistry And Physics*. **16**, 5063-5073 (2016)
- Kok, J., Albani, S., Mahowald, N. & Ward, D. An improved dust emission model—Part 2: Evaluation in the Community Earth System Model, with implications for the use of dust source functions. *Atmospheric Chemistry And Physics*. **14**, 13043-13061 (2014)
- Kumar, R., Barth, M., Pfister, G., Naja, M. & Brasseur, G. WRF-Chem simulations of a typical pre-monsoon dust storm in northern India: 685 influences on aerosol optical properties and radiation budget. *Atmospheric Chemistry And Physics*. **14**, 2431-2446 (2014)
- Labour Inspection, D. Cyprus Air Quality. (2021), Available at: <https://www.airquality.dli.mlsi.gov.cy/graphs>.
- Ladwig, P., Herder, J. & Geiger, C. Towards precise, fast and comfortable immersive polygon mesh modelling: capitalising the results of past research and analysing the needs of professionals. *Proceedings Of The 27th International Conference On Artificial Reality And Telexistence And 22nd Eurographics Symposium On Virtual Environments*. pp. 205-212 (2017)
- 690 Lelieveld, J., Berresheim, H., Borrmann, S., Crutzen, P., Dentener, F., Fischer, H., Feichter, J., Flatau, P., Heland, J., Holzinger, R. & Others Global air pollution crossroads over the Mediterranean. *Science*. **298**, 794-799 (2002)
- Levy, R., Mattoo, S., Munchak, L., Remer, L., Sayer, A., Patadia, F. & Hsu, N. The Collection 6 MODIS aerosol products over land and ocean, *Atmos. Meas. Tech.* **6** pp. 2989-3034, (2013), <https://doi.org/10.5194/amt-6-2989-2013>,
- Logothetis, S., Salamalikis, V., Gkikas, A., Kazadzis, S., Amiridis, V. & Kazantzidis, A. 15-year variability of desert dust optical depth on 695 global and regional scales. *Atmospheric Chemistry And Physics*. **21**, 16499-16529 (2021)
- Lolis, C., Bartzokas, A. & Katsoulis, B. Relation between sensible and latent heat fluxes in the Mediterranean and precipitation in the Greek area during winter. *Int. J. Climatol.* **24** pp. 1803-1816, (2004)
- Lux, O., Lemmerz, C., Weiler, F., Marksteiner, U., Witschas, B., Rahm, S., Geiß, A. & Reitebuch, O. Intercomparison of wind observations from the European Space Agency's Aeolus satellite mission and the ALADIN Airborne Demonstrator. *Atmospheric Measurement 700 Techniques*. **13**, 2075-2097 (2020)
- Mamouri, R. & Ansmann, A. Potential of polarization/Raman lidar to separate fine dust, coarse dust, maritime, and anthropogenic aerosol profiles, *Atmos. Meas. Tech.* **10** pp. 3403-3427, (2017), <https://doi.org/10.5194/amt-10-3403-2017>,
- Marinou, E., Amiridis, V., Biniotoglou, I., Tsikerdekis, A., Solomos, S., Proestakis, E., Konsta, D., Papagiannopoulos, N., Tsekeri, A., Vlastou, G., Zanis, P., Balis, D., Wandinger, U. & Ansmann, A. Three-dimensional evolution of Saharan dust transport towards Europe 705 based on a 9-year EARLINET-optimized CALIPSO dataset, *Atmos. Chem. Phys.* **17**, 5893-5919, (2017)
- Marinou, E., Tesche, M., Nenes, A., Ansmann, A., Schrod, J., Mamali, D., Tsekeri, A., Pikridas, M., Baars, H., Engelmann, R., Voudouri, K., Solomos, S., Sciare, J., Groß, S., Ewald, F. & Amiridis, V. Retrieval of ice-nucleating particle concentrations from lidar observations and comparison with UAV in situ measurements, *Atmos. Chem. Phys.* **19** pp. 11315-11342, (2019), <https://doi.org/10.5194/acp-19-11315-2019>,
- 710 Mehta, M., Singh, R., Singh, A., Singh, N. & Others Recent global aerosol optical depth variations and trends—A comparative study using MODIS and MISR level 3 datasets. *Remote Sensing Of Environment*. **181** pp. 137-150 (2016)
- Middleton, N. & Goudie, A. Saharan dust: sources and trajectories. *Transactions Of The Institute Of British Geographers*. **26**, 165-181 (2001)
- Middleton, N. Desert dust hazards: A global review. *Aeolian Research*. **24** pp. 53-63 (2017)



- 715 Miller, S., Kuciauskas, A., Liu, M., Ji, Q., Reid, J., Breed, D., Walker, A. & Mandoos, A. Haboob dust storms of the southern Arabian Peninsula. *Journal Of Geophysical Research: Atmospheres*. **113** (2008)
- Mona, L., Amodeo, A., Pandolfi, M. & Pappalardo, G. Saharan dust intrusions in the Mediterranean area: Three years of Raman lidar measurements. *Journal Of Geophysical Research: Atmospheres*. **111** (2006)
- Morrison, H., Curry, J., Shupe, M. & Zuidema, P. A New Double-Moment Microphysics Parameterization for Application in Cloud and Climate Models. Part II: Single-Column Modeling of Arctic Clouds. *Journal Of The Atmospheric Sciences*. **62** pp. 1678-1693, (2005)
- 720 Musk, L. Systems. (Cambridge University Press,1988)
- Nabavi, S., Haimberger, L. & Samimi, C. Climatology of dust distribution over West Asia from homogenized remote sensing data. *Aeolian Research*. **21** pp. 93-107 (2016)
- Nabavi, S., Haimberger, L. & Samimi, C. Sensitivity of WRF-chem predictions to dust source function specification in West Asia. *Aeolian Research*. **24** pp. 115-131 (2017)
- 725 Notaro, M., Yu, Y. & Kalashnikova, O. Regime shift in Arabian dust activity, triggered by persistent Fertile Crescent drought. *Journal Of Geophysical Research: Atmospheres*. **120**, 10-229 (2015)
- Oreopoulos, L. & Barker, H. Accounting for subgrid-scale cloud variability in a multi-layer 1-D solar radiative transfer algorithm. *Q. J. R. Meteorol. Soc.* **125** pp. 301- 330 (1999)
- Papayannis, A., Balis, D., Amiridis, V., Chourdakis, G., Tsaknakis, G., Zerefos, C., Castanho, A., Nickovic, S., Kazadzis, S. & Grabowski, J. Measurements of Saharan dust aerosols over the Eastern Mediterranean using elastic backscatter-Raman lidar, spectrophotometric and satellite observations in the frame of the EARLINET project. *Atmospheric Chemistry And Physics*. **5**, 2065-2079 (2005)
- 730 Parajuli, S., Stenchikov, G., Ukhov, A. & Kim, H. Dust emission modeling using a new high-resolution dust source function in WRF-Chem with implications for air quality. *Journal Of Geophysical Research: Atmospheres*. **124**, 10109-10133 (2019)
- Pérez, C., Nickovic, S., Pejanovic, G., Baldasano, J. & Özsoy, E. Interactive dust-radiation modeling: A step to improve weather forecasts. *Journal Of Geophysical Research: Atmospheres*. **111** (2006)
- 735 Pinterits, M., Ullrich, B., Wankmüller, R. & Mareckova, K. Inventory review 2021. Review of emission data reported under the LRTAP Convention and NEC Directive. *Stage 1 And 2 Review. Status Of Gridded And LPS Data*. (2021)
- Pisso, I., Sollum, E., Grythe, H., Kristiansen, N., Cassiani, M., Eckhardt, S., Arnold, D., Morton, D., Thompson, R., Groot Zwaafink, C. & Others The Lagrangian particle dispersion model FLEXPART version 10.4. *Geoscientific Model Development*. **12**, 4955-4997 (2019)
- 740 Pozzer, A., De Meij, A., Yoon, J., Tost, H., Georgoulias, A. & Astitha, M. AOD trends during 2001–2010 from observations and model simulations. *Atmospheric Chemistry And Physics*. **15**, 5521-5535 (2015)
- Proestakis, E., Amiridis, V., Marinou, E., Georgoulias, A., Solomos, S., Kazadzis, S., Chimot, J., Che, H., Alexandri, G., Biniotoglou, I. & Others Nine-year spatial and temporal evolution of desert dust aerosols over South and East Asia as revealed by CALIOP. *Atmospheric Chemistry And Physics*. **18**, 1337-1362 (2018)
- 745 Prospero, J. Saharan dust transport over the North Atlantic Ocean and Mediterranean: An overview. *The Impact Of Desert Dust Across The Mediterranean*. pp. 133-151 (1996)
- Prospero, J. Long-range transport of mineral dust in the global atmosphere: Impact of African dust on the environment of the southeastern United States. *Proceedings Of The National Academy Of Sciences*. **96**, 3396-3403 (1999)
- Prospero, J., Ginoux, P., Torres, O., Nicholson, S. & Gill, T. Environmental characterization of global sources of atmospheric soil dust identified with the Nimbus 7 Total Ozone Mapping Spectrometer (TOMS) absorbing aerosol product. *Reviews Of Geophysics*. **40**, 2-1 (2002)

- Prospero, J., Landing, W. & Schulz, M. African dust deposition to Florida: Temporal and spatial variability and comparisons to models. *Journal Of Geophysical Research: Atmospheres*. **115** (2010)
- 755 Prospero, J., Collard, F., Molinié, J. & Jeannot, A. Characterizing the annual cycle of African dust transport to the Caribbean Basin and South America and its impact on the environment and air quality. *Global Biogeochemical Cycles*. **28**, 757-773 (2014)
- Randles, C., Silva, A., Buchard, V., Colarco, P., Darmenov, A., Govindaraju, R., Smirnov, A., Holben, B., Ferrare, R., Hair, J., Shinozuka, Y., Flynn, C., Randles, C., Silva, A., Buchard, V., Colarco, P., Darmenov, A., Govindaraju, R., Smirnov, A., Holben, B., Ferrare, R., Hair, J., Shinozuka, Y. & Flynn, C. The MERRA-2 Aerosol Reanalysis, 1980 Onward. *Part I: System Description And Data Assimilation Evaluation*, *J. Climate*. **30** pp. 6823-6850, (2017), <https://doi.org/10.1175/JCLI-D16-0609.1>,
- 760 Ravi, S., D'Odorico, P., Breshears, D., Field, J., Goudie, A., Huxman, T., Li, J., Okin, G., Swap, R., Thomas, A. & Others Aeolian processes and the biosphere. *Reviews Of Geophysics*. **49** (2011)
- Rennie, M. & Isaksen, L. Investigations into the Quality of Aeolus L2B Winds Using the ECMWF Model and Initial NWP Impact Assessment. *Living Planet Symposium, Milan, Italy*. pp. 1317 (2019)
- Rennie, M., Isaksen, L., Weiler, F., Kloe, J., Kanitz, T. & Reitebuch, O. The impact of Aeolus wind retrievals on ECMWF global weather forecasts. *Quarterly Journal Of The Royal Meteorological Society*. **147**, 3555-3586 (2021)
- 765 Ridley, D., Heald, C. & Ford, B. North African dust export and deposition: A satellite and model perspective. *Journal Of Geophysical Research: Atmospheres*. **117** (2012)
- Rizza, U., Miglietta, M., Mangia, C., Ielpo, P., Morichetti, M., Iachini, C., Virgili, S. & Passerini, G. Sensitivity of WRF-Chem model to land surface schemes: Assessment in a severe dust outbreak episode in the Central Mediterranean (Apulia Region). *Atmospheric Research*. **201**
- 770 pp. 168-180 (2018)
- Schell, B., Ackermann, I., Hass, H., Binkowski, F., Ebel, A. & B. Modeling the formation of secondary organic aerosol within a comprehensive air quality model system". *Journal Of Geophysical Research: Atmospheres*. **106**, 28275-28293 (2001)
- Schepanski, K., Tegen, I., Todd, M., Heinold, B., Bönisch, G., Laurent, B. & Macke, A. Meteorological processes forcing Saharan dust emission inferred from MSG-SEVIRI observations of subdaily dust source activation and numerical models. *Journal Of Geophysical Research: Atmospheres*. **114** (2009)
- 775 Shaheen, A., Wu, R., Lelieveld, J., Yousefi, R. & Aldabash, M. Winter AOD trend changes over the Eastern Mediterranean and Middle East region. *International Journal Of Climatology*. **41**, 5516-5535 (2021)
- Shimizu, A., Sugimoto, N., Matsui, I., Arai, K., Uno, I., Murayama, T., Kagawa, N., Aoki, K., Uchiyama, A. & Yamazaki, A. Continuous observations of Asian dust and other aerosols by polarizationlidars in China and Japan during ACE-Asia, *J. Geophys. Res.*, **109**, D19S17.
- 780 (2004)
- Shipley, S., Tracy, D., Eloranta, E., Trauger, J., Sroga, J., Roesler, F. & Weinman, J. High spectral resolution lidar to measure optical scattering properties of atmospheric aerosols. 1: Theory and instrumentation. *Applied Optics*. **22**, 3716-3724 (1983)
- Sinyuk, A., Holben, B., Eck, T., Giles, D., Slutsker, I., Korkin, S., Schafer, J., Smirnov, A., Sorokin, M. & Lyapustin, A. The AERONET Version 3 aerosol retrieval algorithm, associated uncertainties and comparisons to Version 2. *Atmospheric Measurement Techniques*. **13**,
- 785 3375-3411 (2020)
- Stefanski, R. & Sivakumar, M. Impacts of sand and dust storms on agriculture and potential agricultural applications of a SDSWS. *IOP Conference Series: Earth And Environmental Science*. **7**, 012016 (2009)
- Stockwell, W., Kirchner, F., Kuhn, M. & Seefeld, S. A new mechanism for regional atmospheric chemistry modeling. *Journal Of Geophysical Research*. **102** pp. 25 847, (1997)

- 790 Stoffelen, A., Pailleux, J., Källén, E., Vaughan, J., Isaksen, L., Flamant, P., Wergen, W., Andersson, E., Schyberg, H., Culoma, A. & Others  
The atmospheric dynamics mission for global wind field measurement. *Bulletin Of The American Meteorological Society*. **86**, 73-88 (2005)
- Stohl, A., Forster, C., Frank, A., Seibert, P. & Wotawa, G. The Lagrangian particle dispersion model FLEXPART version 6.2. *Atmospheric  
Chemistry And Physics*. **5**, 2461-2474 (2005)
- 795 Su, L. & Fung, J. Sensitivities of WRF-Chem to dust emission schemes and land surface properties in simulating dust cycles during springtime  
over East Asia. *Journal Of Geophysical Research: Atmospheres*. **120**, 11-215 (2015)
- Sugimoto, N., Uno, I., Nishikawa, M., Shimizu, A., Matsui, I., Dong, X., Chen, Y. & Quan, H. Record heavy Asian dust in Beijing in 2002:  
Observations and model analysis of recent events. *Geophys. Res.Lett.*, **30**(12) (2003)
- Tegen, I., Schepanski, K. & Heinold, B. Comparing two years of Saharan dust source activation obtained by regional modelling and satellite  
observations. *Atmospheric Chemistry And Physics*. **13**, 2381-2390 (2013)
- 800 Tesche, M., Ansmann, A., Müller, D., Althausen, D., Engelmann, R., Freudenthaler, V. & Groß, S. Vertically resolved separation of dust and  
smoke over Cape Verde using multiwavelength Raman and polarization lidars during Saharan Mineral Dust Experiment 2008. *Journal Of  
Geophysical Research: Atmospheres*. **114** (2009)
- Todd, M., Washington, R., Martins, J., Dubovik, O., Lizcano, G., M'baïnayel, S. & Engelstaedter, S. Mineral dust emission from the Bodélé  
Depression, northern Chad, during BoDEx 2005. *Journal Of Geophysical Research: Atmospheres*. **112** (2007)
- 805 Toledano, C., Cachorro, V., Berjon, A., De Frutos, A., Sorribas, M., Morena, B. & Goloub, P. Aerosol optical depth and Ångström exponent  
climatology at El Arenosillo AERONET site (Huelva, Spain). *Quarterly Journal Of The Royal Meteorological Society: A Journal Of The  
Atmospheric Sciences, Applied Meteorology And Physical Oceanography*. **133**, 795-807 (2007)
- Trigo, R., Trigo, I., DaCamara, C. & Osborn, T. impact of the European winter blocking episodes from the NCEP/NCAR reanalyses. *Climate  
Dyn.* **23** pp. 17-28, (2004)
- 810 Tsarpalis, K., Papadopoulos, A., Mihalopoulos, N., Spyrou, C., Michaelides, S. & Katsafados, P. The implementation of a mineral dust wet  
deposition scheme in the GOCART-AFWA module of the WRF model. *Remote Sensing*. **10**, 1595 (2018)
- Tyrlis, E., Škerlak, B., Sprenger, M., Wernli, H., Zittis, G. & Lelieveld, J. On the linkage between the Asian summer monsoon and tropopause  
fold activity over the eastern Mediterranean and the Middle East. *Journal Of Geophysical Research: Atmospheres*. **119**, 3202-3221 (2014)
- Ukhov, A., Mostamandi, S., Da Silva, A., Flemming, J., Alshehri, Y., Shevchenko, I. & Stenchikov, G. Assessment of natural and anthro-  
pogenic aerosol air pollution in the Middle East using MERRA-2, CAMS data assimilation products, and high-resolution WRF-Chem  
815 model simulations. *Atmospheric Chemistry And Physics*. **20**, 9281-9310 (2020)
- Uno, I., Wang, Z., Chiba, M., Chun, Y., Gong, S., Hara, Y., Jung, E., Lee, S., Liu, M., Mikami, M. & Others Dust model intercomparison  
(DMIP) study over Asia: Overview. *Journal Of Geophysical Research: Atmospheres*. **111** (2006)
- Washington, R. & Todd, M. Synoptic and dynamic aspects of an extreme springtime Saharan dust outbreak. *Geophys. Res. Lett.* **32** (2005)
- 820 Weinzierl, B., Sauer, D., Minikin, A., Reitebuch, O., Dahlkötter, F., Mayer, B., Emde, C., Tegen, I., Gasteiger, J., Petzold, A. & Others On  
the visibility of airborne volcanic ash and mineral dust from the pilot's perspective in flight. *Physics And Chemistry Of The Earth, Parts  
A/B/C*. **45** pp. 87-102 (2012)
- Willmott, C., Robeson, S., Matsuura, K., C., R., S. & Matsuura, K. A refined index of model performance". *International Journal Of  
Climatology*. **32**, 2088-2094 (2011)
- 825 Witschas, B., Lemmerz, C., Geiß, A., Lux, O., Marksteiner, U., Rahm, S., Reitebuch, O. & Weiler, F. First validation of Aeolus wind  
observations by airborne Doppler wind lidar measurements. *Atmospheric Measurement Techniques*. **13**, 2381-2396 (2020)

- Wu, J., Kurosaki, Y., Shinoda, M. & Kai, K. Regional characteristics of recent dust occurrence and its controlling factors in East Asia. *SOLA*. **12** pp. 187-191 (2016)
- 830 Xu, W., Sun, Y., Wang, Q., Zhao, J., Wang, J., Ge, X., Xie, C., Zhou, W., Du, W., Li, J. & Others Changes in aerosol chemistry from 2014 to 2016 in winter in Beijing: Insights from high-resolution aerosol mass spectrometry. *Journal Of Geophysical Research: Atmospheres*. **124**, 1132-1147 (2019)
- Yuan, T., Chen, S., Huang, J., Zhang, X., Luo, Y., Ma, X. & Zhang, G. Sensitivity of simulating a dust storm over Central Asia to different dust schemes using the WRF-Chem model. *Atmospheric Environment*. **207** pp. 16-29 (2019)
- Zender, C., Newman, D. & Torres, O. Spatial heterogeneity in aeolian erodibility: Uniform, topographic, geomorphic, and hydrologic hypotheses. *Journal Of Geophysical Research: Atmospheres*. **108** (2003)
- 835 Zeng, Z., Chen, S., Natraj, V., Le, T., Xu, F., Merrelli, A., Crisp, D., Sander, S. & Yung, Y. Constraining the vertical distribution of coastal dust aerosol using OCO-2 O<sub>2</sub> A-band measurements. *Remote Sensing Of Environment*. **236** pp. 111494 (2020)
- Zhang, D. & Anthes, R. A high-resolution model of the planetary boundary layer Sensitivity tests and comparisons with SEASAME-79 data. *J Appl. Meteor*. **21** pp. 1594-1609 (1982)
- 840 Zhao, C., Liu, X., Leung, L., Johnson, B., McFarlane, S., Gustafson, W., Fast, J. & Easter, R. The spatial distribution of mineral dust and its shortwave radiative forcing over North Africa: Modeling sensitivities to dust emissions and aerosol size treatments, *Atmospheric Chemistry And Physics*. **10** pp. 8821-8838, (2010), <http://www.atmos-chem-phys.net/10/8821/2010/>,
- Zhao, J., Ma, X., Wu, S. & Sha, T. Dust emission and transport in Northwest China: WRF-Chem simulation and comparisons with multi-sensor observations. *Atmospheric Research*. **241** pp. 104978 (2020)